RESEARCH ARTICLE

The moist parcel-in-cell method for modelling moist convection

David G. Dritschel[1] | Steven J. Böing[2] | Douglas J. Parker[2] | Alan M. Blyth[2,3]

[1]Mathematical Institute, University of St Andrews, UK
[2]School of Earth and Environment, University of Leeds, UK
[3]National Centre for Atmospheric Science, University of Leeds, UK

Correspondence
David G. Dritschel, Mathematical Institute, University of St Andrews, St Andrews KY16 9SS, UK.
E-mail: david.dritschel@st-andrews.ac.uk

We describe a promising alternative approach to modelling moist convection and cloud development in the atmosphere. Rather than using a conventional grid-based approach, we use Lagrangian "parcels" to represent key dynamical and thermodynamical variables. In the prototype model considered, parcels carry vorticity, mass, specific humidity, and liquid-water potential temperature. In this first study, we ignore precipitation, and many of these parcel "attributes" remain unchanged (i.e. are materially conserved). While the vorticity does change following the parcel motion, the vorticity tendency is readily computed and, crucially, unwanted numerical diffusion can be avoided. The model, called "Moist Parcel-In-Cell" (MPIC), is a hybrid approach which uses both parcels and a fixed underlying grid for efficiency: advection (here moving parcels) is Lagrangian whereas inversion (determining the velocity field) is Eulerian. The parcel-based representation of key variables has several advantages: (a) it allows an *explicit* subgrid representation; (b) it provides a velocity field which is *undamped* by numerical diffusion all the way down to the grid scale; (c) it does away with the need for eddy viscosity parametrizations and, in their place, it provides for a natural subgrid parcel mixing; (d) it is *exactly conservative* (i.e. there can be no net loss or gain of any theoretically conserved attribute); and (e) it dispenses with the need to have separate equations for each conserved parcel attribute; attributes are simply labels carried by each parcel. Moreover, the latter advantage increases as more attributes are added, such as the distributions of microphysical properties, chemical composition and aerosol loading.

KEYWORDS
convection, clouds, numerical method

1 | INTRODUCTION

Clouds, convection and moist processes generally pose serious challenges for modelling the Earth's climate and weather (e.g. Holloway *et al.*, 2014; Bony *et al.*, 2015). Such processes involve small-scale interactions which are well beyond the resolution of current global circulation models (GCMs). In particular, accurate resolution of processes influenced or controlled by turbulence in clouds requires model scales of the order of metres (Austin *et al.*, 1985; Blyth *et al.*, 2005; Cooper *et al.*, 2013; Heinze *et al.*, 2015; Seifert *et al.*, 2015), scales which are more than seven orders of magnitude smaller than the global scale!

The large-eddy simulation (LES) method has been used to study cumulus and stratocumulus clouds since the pioneering work of Sommeria (1976) and Deardorff (1980). In LES, the impact of subgrid-scale motions on resolved scales is modelled by turbulence closure assumptions. LES models play a key role in the development of low cloud parametrizations (e.g. Siebesma and Cuijpers, 1995) and have been routinely validated for observational cases (e.g. Brown *et al.*, 2002; Siebesma *et al.*, 2003). Other non-hydrostatic

models have also been essential in studying the interaction between deep convection and its environment (e.g. Bretherton and Smolarkiewicz, 1989), and mixing at the edge of clouds (Grabowski and Clark, 1993). However, there are key differences between two-dimensional and three-dimensional simulations of deep convection (Redelsperger *et al.*, 2000; Petch *et al.*, 2008), and three-dimensional LES on large domains has only become possible over the last decade (Khairoutdinov *et al.*, 2009). Detailed cloud models have also been used both as embedded models for local weather forecasting (Schalkwijk *et al.*, 2015) or as subgrid models in larger-scale models ("super-parametrization," e.g. Grabowski and Smolarkiewicz, 1999).

The need for a high-resolution description of cloud turbulence is due to the highly nonlinear nature of cloud processes. Previous studies have shown that the behaviour of cumulus clouds is very sensitive to the choice of numerical method (Matheou, 2011; Pressel *et al.*, 2015). The equations of state describing the transfer between different phases of water involve very steep functions, usually represented by discontinuous changes. Furthermore, aircraft measurements have shown that the thermodynamic properties of clouds can have large variations on scales of metres to tens of metres (Austin *et al.*, 1985; Blyth *et al.*, 2005), and cumulus clouds often contain cores with relatively high liquid water content (Heymsfield *et al.*, 1978; Blyth *et al.*, 2005; 2015; Moser and Lasher-Trapp, 2017). Such regions may be important in determining the time-scale for rain formation (Twomey, 1966; Blyth *et al.*, 2013; Cooper *et al.*, 2013). Resolving these scales of motion appears to be essential to modelling cumulus convection.

The computational demands for high-resolution cloud simulation are exacerbated when consideration is made of additional attributes of the air parcels, such as the distributions of microphysical properties (e.g. drop sizes), chemical composition and aerosol loading. Accurate treatment of cloud microphysics demands consideration of droplet size distributions of cloud water and cloud ice distributions: the ice is itself divided into many possible classes (according to crystal form, aggregation, etc). For instance, a model may carry $N \sim 6$ species of water and ice with $M \sim 50$ bins. Clouds are also important agents of transport and chemical transformation of trace gases in the climate system, and many of the chemical reactions are nonlinear and occur on the fine scales within a cloud. Sophisticated cloud-chemistry schemes may include many interacting species. Aerosols feed back on the cloud physics by acting as condensation nuclei and modifying the distributions of cloud particles. For these reasons, a sophisticated cloud-resolving model capable of studying cloud–chemistry–climate processes may need to carry cloud microphysical spectra, aerosol spectra and a number of interacting chemical species on its grids. These additional attributes place enormous demands on computational resources – involving *both* the cost of dynamical transport *and* that of additional processes such as chemical reactions – and

are included at the expense of the resolution needed to capture cloud fine structure.

There is hence a pressing need to improve the numerical modelling and representation of moist processes in general. Previous studies have considered whether methods used in the computer graphics and gaming community can help to provide simulations with a higher effective resolution at reduced computational cost (e.g. Shutts and Allen, 2007). In this paper, we also propose a non-standard approach, namely to represent dynamical and thermodynamic processes by freely moving *parcels*. The parcels carry a number of attributes, such as vorticity, mass, specific humidity, and liquid-water potential temperature. Ignoring precipitation, the attributes of mass, specific humidity and liquid-water potential temperature are all conserved following the motion of each parcel, and importantly a parcel-based model guarantees this *without* the need to follow additional prognostic equations as in a conventional numerical model. The advantages grow when more attributes are considered, such as a spectrum of aerosol particle sizes, chemical species, etc. Moreover, the parcels provide an explicit sub-grid parametrization – indeed they replace the need for such a parametrization – thereby dispensing with *ad hoc* parametrizations and artificial "eddy" viscosities. Mixing on the smallest scales can be dealt with by parcels splitting and recombining. *A priori*, a parcel-based model has much less numerical dissipation than conventional numerical models presently in widespread use. Hence, a parcel-based model can be expected to achieve a much higher effective resolution.

Parcel-based methods are not new: they have been used in the vortex dynamics literature for decades to study basic properties of fluid flows at very high Reynolds numbers (e.g. Christiansen and Zabusky, 1973 for two-dimensional flows, and Novikov, 1983, Aksman *et al.*, 1985, Anderson and Greengard, 1985, Alkemade *et al.*, 1993 for three-dimensional flows). Such methods have even been used to model moist convection as early as Gadian (1991), who simulated clouds in a two-dimensional plane using Smoothed Particle Hydrodynamics (SPH). This method in fact originated in studies of astrophysical phenomena (Monaghan, 1992), and continues to be a popular choice in modelling galaxy dynamics, star formation and stellar clusters (e.g. Smilgys and Bonnell, 2017). In atmospheric chemistry and transport studies, parcel-based methods such as the Finite Mass Method (FMM; Klinger *et al.*, 2005 and references therein) and the Hamiltonian Particle-Mesh method (HPM; Frank *et al.*, 2002) have been shown to offer significant improvements over the commonly used grid-based semi-Lagrangian method (Grewe *et al.*, 2014). The HPM method uses particles rather than parcels of finite volume, and uses a spatial smoothing kernel for the interpolation of particle properties to an underlying grid. This is done in a consistent way to ensure conservation of properties such as total mass, etc. Parcel and particle-based methods have also been used to model cloud and rain water in combination with

a dynamical core that is otherwise Eulerian (e.g. Andrejczuk *et al.*, 2008; Shima *et al.*, 2009; Riechelmann *et al.*, 2012; Wyszogrodzki *et al.*, 2013). Nevertheless, to our knowledge, a parcel-based method has never been seriously considered to be a viable approach for detailed cloud modelling.

Parcel and particle-based methods vary considerably in their formulation, and may require the tuning of many numerical parameters. We believe that this has detracted from the uptake of such methods by the atmospheric modelling community. Here, in order to produce a flexible, versatile model with a minimum of tunable parameters, we adopt the simplest "vortex-in-cell" (VIC) approach of Christiansen and Zabusky (1973), with a parameter-free refinement due to Brackbill and Ruppel (1986) to ensure conservation. We also use the mathematically reformulated parcel vorticity equation of Cottet and Koumoutsakos (2000, pp. 244–245) to more accurately satisfy the non-divergence condition of the vorticity field. Moist processes, specifically the effects of condensation and evaporation, are incorporated in a simplified way and in an idealized physical setting, with the sole purpose of providing a proof of concept.

The resulting new model, called "Moist Parcel-In-Cell" (MPIC), is extensively tested to understand dependencies on numerical parameters and to determine feasible values. As a demanding test case, we consider the evolution of a rising moist thermal in a neutral layer below a stratified zone. The thermal reaches the stratified zone and passes through the lifting condensation level where it releases additional buoyancy and forms a cloud. The flow evolution rapidly becomes turbulent, and is reminiscent of observed cumulus convection. Comparisons with a convection-permitting research model, the Met-Office/NERC cloud model (MONC) are the focus of a forthcoming paper (Böing *et al.*, forthcoming). There, and in one figure here, the MPIC model is shown to compare well using significantly lower grid resolutions. This is the result of using a conservative sub-grid representation in the MPIC model, thereby greatly reducing the effects of numerical diffusion.

The plan of the paper is as follows. Section 2 describes the idealized physical setting considered, and sets out the associated simplified mathematical model. Section 3 then details the MPIC numerical method, focussing in particular on its novel or non-standard features. Section 4 goes through a series of tests which demonstrate the insensitivity of the results to the only tunable parameters, those controlling parcel density and mixing. Finally, section 5 concludes with a discussion of the steps currently being taken to extend the MPIC model to more realistic physical settings.

2 | PHYSICAL SETTING AND MATHEMATICAL FRAMEWORK

Cloud formation in the atmosphere is a highly complex process. We do not attempt to model every aspect of this process, but only intend to demonstrate a viable computational approach that could lead to a step change in modelling atmospheric convection in general. To this end, we consider a simplified physical setting in an idealized geometry, and reduce the governing mathematical equations to their simplest relevant form. Key aspects of the dynamics and physics are retained, notably the inclusion of a latent heating term with a nonlinearity characteristic of more sophisticated cloud schemes.

First, we assume the domain is Cartesian, horizontally periodic in x ($0 \leq x \leq L_x$) and in y ($0 \leq y \leq L_y$), and bounded below and above by flat, impermeable, free-slip surfaces at $z = 0$ and L_z. Second, we make the incompressible Boussinesq approximation (Durran and Arakawa, 2007) in which variations in density are small compared with the domain average density. This is not valid for deep convection, but is often used in studies of shallow convection (Brown *et al.*, 2002; Siebesma *et al.*, 2003). This approximation greatly simplifies the governing equations, but it is not required by the MPIC model (section 5 below). Third, we simplify the pressure–temperature dependent formulation of saturation specific humidity occurring when moisture within an air parcel condenses or evaporates. Instead, the effects of latent heating are included by increasing the parcel buoyancy b whenever the parcel specific humidity q exceeds a height-dependent background profile $q_0 e^{-\lambda z}$ (with λ constant). Effectively, the saturation specific humidity depends only on height. Thus, a moist parcel can gain buoyancy (tending to accelerate upwards) when its water vapour condenses. Likewise, it can lose buoyancy when it evaporates. Condensational heating is the only effect of moisture that we account for: we ignore differences in density between dry air and water vapour, as well as the weight/loading of condensate.

The simplicity of this framework has been designed so that the first development of the model, and the analysis of its performance, focusses on the essentially Lagrangian dynamical core. In particular, we have constructed a model framework which is simple enough to isolate the dynamical behaviour without additional complicating processes, such as microphysical feedbacks. In this framework, we are able to characterize the dynamical performance quantitatively and definitively. The simple framework will make it easy for others to replicate our results, and it also ensures the equations lend themselves to non-dimensionalization. The key feature of the thermodynamics that we have retained is the discontinuity in the equation of state that is a result of condensation. There are some precedents for making the saturation specific humidity depend on height only: for example, Pierrehumbert *et al.* (2007) and Tsang and Vanneste (2017) essentially use the same formulation. However, in their case, liquid water is assumed to be removed (precipitate), whereas in our case liquid water does not precipitate but can re-evaporate.

Another example of the use of a simplified equation of state is the approach of Pauluis and Schumacher (2010). Their formulation comes closer to the full equation of state for small

domain heights, as the liquid water content here depends on height as well as two other thermodynamic variables. However, the interpretation of the thermodynamic variables in this framework is less straightforward. Moreover, once a parcel is saturated, the amount of condensation per unit height is constant rather than exponentially decreasing in this formulation, which makes it less appropriate for deeper domains.

Our ongoing work in the development of the model will add increasing degrees of sophistication to the microphysical representations. It would be relatively simple to replace our thermodynamic formulation with a saturation specific humidity which depends on temperature and a height-dependent reference pressure. In this case, we would need to include an iterative procedure for solving the equation of state. Usually, some simplifications are made in the thermodynamics, and different models use a variety of formulations. The details do not matter for a proof of concept, and this is why we have taken the simplest approach.

The governing equations written in momentum form for velocity $\mathbf{u}$, (non-hydrostatic) pressure p, liquid-water buoyancy b_l and specific humidity q are

$$\frac{D\mathbf{u}}{Dt} = -\frac{\nabla p}{\rho_0} + b\,\hat{\mathbf{e}}_z, \tag{1}$$

$$\frac{Db_l}{Dt} = 0, \tag{2}$$

$$\frac{Dq}{Dt} = 0, \tag{3}$$

$$\nabla \cdot \mathbf{u} = 0, \tag{4}$$

where $D/Dt = \partial/\partial t + \mathbf{u} \cdot \nabla$ is the material derivative. In Equation 1 the total buoyancy b (including the effects of latent heating) is approximated by

$$b = b_l + \frac{gL}{c_p \theta_{l0}} q_c, \tag{5}$$

where

$$q_c = \max\left(0, q - q_0 e^{-\lambda z}\right) \tag{6}$$

is the liquid water content. The pressure p in Equation 1 excludes the part due to the hydrostatic background state of constant density ρ_0. The other symbols appearing in Equations 1–6 are the vertical unit vector $\hat{\mathbf{e}}_z$, the gravitational acceleration g, the latent heat of condensation L, the specific heat at constant pressure c_p, the surface saturation humidity q_0, and the inverse condensation scale-height λ. The liquid-water buoyancy is defined by $b_l = g(\theta_l - \theta_{l0})/\theta_{l0}$ where θ_l is the liquid-water potential temperature and θ_{l0} is a constant reference value.

The incompressible Boussinesq approximation is convenient since, in the vorticity formulation, the pressure term disappears. The vorticity $\boldsymbol{\omega} = \nabla \times \mathbf{u}$ satisfies

$$\frac{D\boldsymbol{\omega}}{Dt} = \boldsymbol{\omega} \cdot \nabla \mathbf{u} + \left(b_y, -b_x, 0\right), \tag{7}$$

where subscripts on b denote partial differentiation. Hence, vorticity is generated by horizontal buoyancy gradients.

Notably, regions of the flow with uniform b and no vorticity remain irrotational ($\boldsymbol{\omega} = 0$).

Small-scale models of deep convection usually employ an anelastic formulation of the continuity equation (Pauluis, 2008) rather than the incompressible Boussinesq approximation we are using here. In the near future, we aim to extend MPIC to the anelastic framework by weighting both its conserved properties and the parcel volumes by a height-dependent mean density $\rho_0(z)$, and by making appropriate changes to the numerical solver. To use MPIC as an embedded model, it would also be important to ensure maximum consistency in the thermodynamical formulation with the host model (Grabowski and Smolarkiewicz, 2002).

Finally, we ignore precipitation. However, the Lagrangian method for precipitation introduced by Shima *et al.* (2009) would be one of the ways in which this could be added. We plan to include precipitation in a future version of MPIC.

3 | THE NUMERICAL ALGORITHM

We first present an overview of the algorithm, then describe how it is constructed and provide details of features not found in other parcel-based numerical methods.

Lagrangian, freely-moving parcels are used for evolving all quantities, while an underlying regular (here Cartesian) grid is used for transferring parcel properties to the grid and *vice versa*. The grid is also used for "inversion," i.e. to obtain the velocity field from the interpolated vorticity field. This is the basis for the original Vortex-In-Cell (VIC) method (see Christiansen and Zabusky, 1973 and the comprehensive review of Cottet and Koumoutsakos, 2000). The parcels are ideal for carrying quantities which do not change in time – materially conserved quantities called "attributes." In the present model, the attributes consist of liquid-water buoyancy b_l, specific humidity q and parcel volume V. No additional equations are required to evolve the attributes as in a grid-based model; the attributes are merely labels carried by each parcel. Instead, the positions $\mathbf{x}_i$ of each parcel i are evolved using the simple equation

$$\frac{d\mathbf{x}_i}{dt} = \mathbf{u}(\mathbf{x}_i, t), \tag{8}$$

where $\mathbf{u}$ is the gridded velocity field interpolated at $\mathbf{x}_i$. An additional vector equation is required to update the parcel vorticity $\boldsymbol{\omega}_i$, which changes as a result of both vortex stretching and horizontal buoyancy gradients (section 3.1 below). The parcel vorticity is itself an odd concept since, by definition, vorticity must be divergence-free ($\nabla \cdot \boldsymbol{\omega} = 0$; discussion in Cottet and Koumoutsakos, 2000, pp. 84–85). A dense collection of parcels can approximate this condition, but one can also regard the field generated by all parcels as only part of the entire vorticity field $\boldsymbol{\omega}$. The remaining part (which has the form of a gradient of a potential—section 3.1 gives further explanation) can be chosen to satisfy $\nabla \cdot \boldsymbol{\omega} = 0$.

But what is most remarkable is that this remaining part contributes nothing to the velocity field (though it is needed in the vorticity tendency equation).

A potential drawback of parcel-based methods is that large numbers of parcels must be superposed to accurately represent any evolving flow. In the original applications to a uniform density fluid, parcels could be restricted to a small volume of the entire space, as in that case no new vorticity is produced outside of its initial domain of support. In a variable-density flow, vorticity does not remain localized if initially so. Hence, in the MPIC model, we fill the *entire* domain with parcels, ensuring each grid box contains many parcels (typically 5–200). We originally thought this would be computationally prohibitive, but it turns out to be affordable, especially when compared to conventional numerical models. Essentially, we have found that the higher effective resolution afforded by the parcels – and the strict conservation of parcel attributes – strongly offsets the costs of carrying a large number of space-filling parcels. The operations performed on parcels are mostly simple interpolations (see below) which are relatively inexpensive from a computational point of view.

Another well-known problem with parcel methods is that the parcel motion does not respect exact mass conservation or incompressibility (Grewe *et al.*, 2014). While each parcel carries a volume, and the parcel advection is accurate, using a finite number of parcels inevitably leads to numerical density anomalies, even if care is taken initially to ensure a perfect match between the parcel and grid densities (or volumes in an incompressible flow). This problem can be alleviated by conservatively adjusting parcel properties (e.g. as in Grewe *et al.*, 2014), but its seriousness depends on the number of parcels used to find a given field on the grid, and the duration of the flow simulation. Grabowski *et al.* (2018) describe a scheme in which the interpolated velocity field is incompressible throughout each grid box, but even this does not guarantee that the parcel density remains uniform (as the example of a single parcel crossing a grid box boundary demonstrates). In the results presented below using the MPIC model, we find that the discrepancy between parcel and grid densities is negligible over cloud development time-scales when using the recommended default numerical settings.

Parcels simplify many features of the dynamics. In particular, the effects of condensation and evaporation on parcel buoyancy are naturally incorporated in a parcel formulation. All that is required is to construct the total buoyancy b from the liquid-water buoyancy b_l, specific humidity q and parcel height z using Equation 5, then interpolate b to gridded values for calculating the parcel vorticity tendencies (section 3.1).

The MPIC model uses perhaps the simplest of all interpolations – tri-linear interpolation – to transfer parcel properties to and from an underlying grid. This interpolation is needed in order to build the vorticity field on a grid and to use efficient, accurate grid-based methods for calculating the velocity field from the vorticity field. The gridded velocity field is then interpolated at the parcel positions, enabling one to move the parcels forward to the next instant of time. Other forms of interpolation (e.g. involving a search over nearby parcels as in SPH or HPM) may be more accurate, but are not nearly as simple, and may not lend themselves to efficient calculation on massively parallel computers. Notably, the interpolation used ensures that the total parcel mass, and indeed all parcel attributes, are not only conserved but are identical to the grid-based calculation of the same quantities after interpolation (Brackbill and Ruppel, 1986; Cottet and Koumoutsakos, 2000, pp. 241–242).

In order to follow the inevitable, and often rapid, cascade of scales in a turbulent flow, we allow for parcel splitting down to a prescribed minimum scale. To decide when parcels should split, we keep track of each parcel's "stretch": the time integral of the magnitude of the vortex stretching. (Note: a more robust measure of parcel stretch would make use of the local strain tensor $\nabla \mathbf{u}$, but this requires tracking the parcel shape (five extra variables) as in McKiver and Dritschel, 2003.) When the stretch exceeds a certain threshold (around four in practice, though the results are insensitive to this, as shown in section 4), we split the parcel into two adjacent pieces, each with half the volume of the original parcel but with identical attributes and vorticity. This splitting is designed to be fully conservative: the total volume-integrated parcel attributes do not change.

However, splitting cannot be allowed to carry on indefinitely, as it would lead to an explosive build-up in the total number of parcels. Hence, we limit the volume of the smallest parcel to $1/6^3$ or $1/216$ of the grid-box volume, and remove smaller parcels conservatively (section 3.5 below). Again, the accuracy of the model is not sensitive to this parameter as long as it is substantially smaller than the original parcel volume (as shown in section 4).

The principle behind this is that there is a trade-off between representing subgrid-scale effects and ignoring subgrid-scale velocity fluctuations (in the interpolation of parcel velocities from gridded values). Parcel motions are generally dominated by the larger-scale velocity field, but this cannot be expected to hold for too great a separation between the parcel size and the grid size. Nonetheless, a subgrid representation may be highly beneficial, as has been demonstrated in contour-based, Lagrangian simulations of two-dimensional fluid and magnetized turbulence (Dritschel and Ambaum, 1997; Dritschel and Scott, 2009; Fontane and Dritschel, 2009; Dritschel and Fontane, 2010; Dritschel and Tobias, 2012).

In two dimensions, velocity fluctuations tend to decay more rapidly with decreasing scale than in three dimensions. The kinetic energy spectral density $\mathcal{K}(k)$ in two dimensions often exhibits a k^{-3} form for large wavenumber k, while in three dimensions $\mathcal{K}(k) \sim k^{-5/3}$ (Davidson, 2015). As $\mathcal{K}(k) \propto k\|\hat{\mathbf{u}}\|^2$, this means that velocity fluctuations $\|\hat{\mathbf{u}}\|$ typically decay like k^{-2} in two dimensions and like $k^{-4/3}$ in three dimensions. In either case, the large scales dominate the

velocity field, but the small scales are much more active in three dimensions.

Previous studies of two-dimensional turbulence conducted using contour-based Lagrangian methods have shown that the scale separation between the finest resolved Lagrangian element and the grid scale can be as large as a factor of 16, while still faithfully representing the flow field (in particular, Dritschel and Scott, 2009 and Dritschel and Tobias, 2012). In the present context, in three dimensions, we do not expect such a large scale separation, and our choice of a factor of 6 is explained and justified in the results below.

As in parcel splitting, we ensure parcel removal is exactly conservative. Each parcel transfers its vorticity and attributes to the corners of the grid box containing it before it is removed. These residuals are then re-interpolated to the remaining parcels to ensure conservation. Notably, this acts as a weak diffusion: a localized parcel disperses its properties to all other parcels in its grid box *as well as* in the grid boxes adjacent to this grid box.

3.1 | The parcel vorticity equation

The parcel vorticity $\boldsymbol{\omega}_i$ is updated using a mathematically equivalent form of the vorticity equation 7 applied to each parcel:

$$\frac{d\boldsymbol{\omega}_i}{dt} = \mathbf{S}(\mathbf{x}_i, t), \tag{9}$$

where

$$\mathbf{S}(\mathbf{x}, t) \equiv (\boldsymbol{\nabla} \cdot \mathbf{F}, \boldsymbol{\nabla} \cdot \mathbf{G}, \boldsymbol{\nabla} \cdot \mathbf{H}) \tag{10}$$

is the vorticity tendency, and

$$\mathbf{F} = \boldsymbol{\omega}u + b\widehat{\mathbf{e}}_y, \quad \mathbf{G} = \boldsymbol{\omega}v - b\widehat{\mathbf{e}}_x, \quad \mathbf{H} = \boldsymbol{\omega}w. \tag{11}$$

In Equation 11, $\widehat{\mathbf{e}}_x$ and $\widehat{\mathbf{e}}_y$ are unit vectors in the x and y directions respectively.

The vorticity tendency $\mathbf{S}$ is first found on the grid and then interpolated to the parcel positions. Since $\boldsymbol{\nabla} \cdot \boldsymbol{\omega} = 0$, this tendency is equivalent to that on the r.h.s. of Equation 7. This form of the tendency is used because it better preserves $\boldsymbol{\nabla} \cdot \boldsymbol{\omega}_p = 0$ for the parcel-interpolated vorticity field $\boldsymbol{\omega}_p$ (Cottet and Koumoutsakos, 2000, pp. 244–245), as we have ourselves verified. However $\boldsymbol{\omega}_p$ does not generally satisfy the solenoidal condition (which should hold if $\boldsymbol{\omega}_p = \boldsymbol{\nabla} \times \mathbf{u}$). This discrepancy can be removed by finding a scalar potential $\chi(\mathbf{x}, t)$ for which $\boldsymbol{\omega} \equiv \boldsymbol{\omega}_p - \boldsymbol{\nabla}\chi$ is solenoidal. This implies $\nabla^2\chi = \boldsymbol{\nabla} \cdot \boldsymbol{\omega}_p$. So, while $\boldsymbol{\omega}_p$ may be localized on a parcel, $\boldsymbol{\omega}$ is generally not. One may think of $\boldsymbol{\nabla}\chi$ as the field that threads all the parcels together to ensure vortex lines never end in the fluid. Remarkably, $\boldsymbol{\nabla}\chi$ does not contribute to the gridded velocity field $\mathbf{u}$, as shown in section 3.3.

3.2 | Parcel interpolation

We next briefly describe the (mostly) standard means of transferring parcel properties to the underlying grid, and the inverse operation of interpolating grid properties at a parcel position. In this subsection, a subscript i denotes a parcel quantity while an overbar as in $\bar{q}$ denotes a gridded field.

In the MPIC model, both of these operations use tri-linear interpolation, a simple method based on dividing a grid box into sub-volumes which are then used as weights in the interpolation. For example, the gridded value of the specific humidity, $\bar{q}(\bar{\mathbf{x}}, t)$, at each grid point $\bar{\mathbf{x}} = (\bar{x}, \bar{y}, \bar{z})$ is computed from

$$\bar{q}(\bar{\mathbf{x}}, t) = \bar{V}^{-1} \sum_{i \in \mathcal{P}(\bar{\mathbf{x}})} \phi(\mathbf{x}_i - \bar{\mathbf{x}})q_i V_i \tag{12}$$

$$\text{with} \quad \bar{V}(\bar{\mathbf{x}}, t) = \sum_{i \in \mathcal{P}(\bar{\mathbf{x}})} \phi(\mathbf{x}_i - \bar{\mathbf{x}})V_i, \tag{13}$$

where the tri-linear weights ϕ are given by

$$\phi(\mathbf{x}_i - \bar{\mathbf{x}}) =$$
$$\left(1 - \frac{|x_i - \bar{x}|}{\Delta x}\right)\left(1 - \frac{|y_i - \bar{y}|}{\Delta y}\right)\left(1 - \frac{|z_i - \bar{z}|}{\Delta z}\right) \tag{14}$$

and $\mathcal{P}(\bar{\mathbf{x}})$ is the set of all parcels within the eight grid boxes surrounding $\bar{\mathbf{x}}$. Here Δx, Δy and Δz are the grid lengths in the three coordinate directions. This interpolation scheme preserves the global integral of q as well as its first moments (integrals of xq, yq and zq). Moreover, compared to the original VIC interpolation scheme that used $\bar{V} = \Delta V$, where $\Delta V \equiv \Delta x \Delta y \Delta z$ is the grid box volume, this scheme has the advantage that the variance of q is non-increasing (Brackbill and Ruppel, 1986; Cottet and Koumoutsakos, 2000, pp. 241–242).

In practice, it is not necessary to find the set $\mathcal{P}(\bar{\mathbf{x}})$ directly; instead we sum over all parcels i and work out the grid box they are contained within. From this, we add appropriately weighted parcel properties to the eight corner grid points.

After interpolation, the volumes $\bar{V}(\bar{\mathbf{x}}, t)$ of boundary grid points (at $z = 0$ and L_z) are doubled since these grid points are surrounded by only four grid boxes rather than eight in the interior. Similarly, the sum in Equation 12 is either doubled or set to zero depending on symmetry of the field (section 3.3 below). The buoyancy $\bar{b}$ and specific humidity $\bar{q}$ are set to fixed, uniform values at each boundary to simplify the inversion problem discussed in section 3.3, though this is not essential.

Note that, in an incompressible fluid, we would expect that $\bar{V}(\bar{\mathbf{x}}, t)$ remains constant and equal to the grid box volume ΔV everywhere. However, Lagrangian parcel advection does not guarantee this. This may be regarded as a source of error, but in practice $\bar{V}(\bar{\mathbf{x}}, t)$ differs little from ΔV if a sufficient number of parcels are used, as the results in section 4 demonstrate. (With a minor change to the algorithm, we can enforce volume conservation, but this comes at the expense of numerical diffusion; section 3.5 below.)

The reverse operation, to interpolate a gridded field value to a parcel position $\mathbf{x}_i(t)$, is performed as follows. For example, the velocity of a parcel is computed from

$$\mathbf{u}(\mathbf{x}_i, t) = \sum_{\bar{\mathbf{x}} \in \mathcal{G}_i} \phi(\mathbf{x}_i - \bar{\mathbf{x}})\,\bar{\mathbf{u}}(\bar{\mathbf{x}}, t), \tag{15}$$

where $\mathcal{G}_i$ is the set of all eight grid points at the corners of the grid box containing parcel i.

3.3 | The inversion problem

Since the domain considered is horizontally periodic, it makes sense to use Fourier series and Fast Fourier Transforms (FFTs) to perform operations on gridded fields. In the vertical, we also use Fourier series, for simplicity, though finite differencing would be more computationally efficient. Fourier series are not necessarily more accurate than second-order finite differences, particularly when fields exhibit shallow spectra, as is typical in turbulent flows (Shipton, 2008). Nonetheless, they allow for the most straightforward computational implementation. In fact, in the MPIC model, *any* solver could be used which provides the velocity field and the vorticity tendency on a regular grid.

Here we discuss how we obtain the (gridded) velocity field **u** from the vorticity field $\boldsymbol{\omega}$ together with appropriate boundary conditions. This is a standard problem, but a few details are provided for clarity. In this subsection, the overbar on gridded quantities is dropped since there is no reference to parcel quantities.

For the incompressible flow considered, we can satisfy $\boldsymbol{\nabla} \cdot \mathbf{u} = 0$ by taking $\mathbf{u} = -\boldsymbol{\nabla} \times \mathbf{A}$ where **A** is a vector potential. From the definition of vorticity and basic vector calculus, we find

$$\boldsymbol{\omega} = \boldsymbol{\nabla} \times \mathbf{u} = \nabla^2 \mathbf{A} - \boldsymbol{\nabla}(\boldsymbol{\nabla} \cdot \mathbf{A}). \tag{16}$$

We are free to impose $\boldsymbol{\nabla} \cdot \mathbf{A} = 0$ leading to

$$\boldsymbol{\omega} = \nabla^2 \mathbf{A}, \tag{17}$$

a (vector) Poisson equation to determine $\mathbf{A} = (A, B, C)$ from $\boldsymbol{\omega} = (\xi, \eta, \zeta)$. To solve this, we must account for the boundary conditions at $z = 0$ and L_z. First of all, the vertical velocity component w must vanish. The horizontal components u and v may be arbitrary (free slip). As $u = B_z - C_y$, $v = C_x - A_z$, $w = A_y - B_x$ and $\boldsymbol{\nabla} \cdot \mathbf{A} = A_x + B_y + C_z = 0$, it is then sufficient to take $A = B = C_z = 0$ on each boundary.

Because we use Fourier series in z, we represent A and B as a sine series, and C as a cosine series. It is most straightforward to represent the vorticity components in the same way, which then implies $\xi = \eta = \zeta_z = 0$ on each boundary (note $\xi = -v_z$ and $\eta = u_z$ there; $u_z = v_z = 0$ is sometimes referred to as a "stress-free" boundary condition). This means vortex lines are perpendicular to each boundary and pass "through" them continuously. But for ξ and η to remain zero on the boundaries, it is necessary to take the buoyancy b to be uniform – then from Equation 7 there is no baroclinic vorticity generation.

If b is initially uniform on each boundary, in the absence of condensation there, b will remain uniform (and constant) due to material conservation of b_l (Equation 2). In the future, we will allow arbitrary b variations to study e.g. localized surface heating and moisture sources. Recovering **u** from $\boldsymbol{\omega}$ in this

case is not as straightforward (cf. Cottet and Koumoutsakos, 2000, pp. 92–96).

In the numerical method, we use Fourier series in x, y and z (with corresponding wavenumbers k_x, k_y and k_z). Depending on the field, either a sine series or a cosine series is used in z to match the required boundary conditions. After an FFT, the Poisson problem Equation 17 reduces to an algebraic one, giving

$$\widehat{\mathbf{A}} = -\widehat{\boldsymbol{\omega}}/|\mathbf{k}|^2 \tag{18}$$

directly, where $\mathbf{k} = (k_x, k_y, k_z)$ and a hat indicates a spectral quantity. Note $\mathbf{k} = 0$ is excluded as the domain-averaged value of $\boldsymbol{\omega}$ is zero. From $\widehat{\mathbf{A}}$, the velocity components in spectral space are found simply by wavenumber multiplication. Finally, an inverse FFT provides the velocity field **u** at all grid points.

The vorticity $\boldsymbol{\omega}$ above includes the correction to the parcel vorticity $\boldsymbol{\omega}_p$ which makes it solenoidal, as discussed above in section 3.1. That is, $\boldsymbol{\omega} \equiv \boldsymbol{\omega}_p - \boldsymbol{\nabla}\chi$ where $\nabla^2 \chi = \boldsymbol{\nabla} \cdot \boldsymbol{\omega}_p$. To solve this Poisson problem, we expand χ and the source $\boldsymbol{\nabla} \cdot \boldsymbol{\omega}_p$ in a Fourier sine series in z and obtain $\widehat{\chi}$ as in Equation 18. Notably this correction does not contribute to the velocity **u** since $\boldsymbol{\nabla} \times \nabla^{-2}\boldsymbol{\nabla}\chi = 0$ for the boundary conditions considered. Nonetheless it is included to more accurately compute the vorticity tendency **S** in Equations 10 and 11.

3.4 | Filtering

A circular de-aliasing filter is applied to avoid spurious modes arising when computing the nonlinear product terms in the vorticity tendency Equation 10. The standard "2/3 rule" is applied, whereby we set to zero all coefficients with wavenumbers greater than 2/3 of the maximum wavenumber (Canuto *et al.*, 2007). Rather than do this in k_x, k_y and k_z separately, we instead apply the circular filter

$$F(k) = \begin{cases} 1 & k < 2k_{\max}/3, \\ 0 & k \geq 2k_{\max}/3, \end{cases} \tag{19}$$

where $k = |\mathbf{k}|$ and $k_{\max} = \sqrt{(n_x^2 + n_y^2 + n_z^2)/6}$. This filter is applied to the vorticity field $\boldsymbol{\omega}$ when it is corrected to be solenoidal. The velocity field **u** is then automatically filtered because of the linear relation between $\boldsymbol{\omega}$ and **u**. No other filtering or damping is used.

3.5 | Parcel splitting and mixing

Turbulent flows exhibit a strong forward cascade of kinetic energy to small scales where the energy is ultimately dissipated or converted to other forms (Davidson, 2015). The range of scales involved in the atmosphere is enormous, and no numerical model is capable of resolving the full range of scales. Inevitably, some form of numerical dissipation or "eddy viscosity" (Meneveau and Katz, 2000; Pope, 2004) must be used to limit this cascade to a restricted range of scales. However, this dissipation invariably degrades the accuracy of the resolved scales of motion.

In the MPIC model, the small-scale end of this cascade is modelled by parcel splitting and eventual removal at a prescribed smallest scale. While we do not follow the shape of each parcel, we do monitor the integrated vorticity stretching

$$\gamma_i(t) = \int_{t_i}^{t} (|\boldsymbol{\omega}_i \cdot \mathrm{d}\boldsymbol{\omega}_i/\mathrm{d}t|)^{1/3} \, \mathrm{d}t, \tag{20}$$

where t_i is the time when the parcel came into existence or last split. Then, when $\gamma_i(t) > \gamma_{\max}$, the parcel is split into two adjacent pieces, each with half the volume of the original parcel but identical vorticity and attributes. Here, $\gamma_{\max}$ is a non-dimensional numerical parameter which must be chosen *a priori*. The default value is $\gamma_{\max} = 4$ but, as shown in section 4, the results are not strongly sensitive to this choice. A smaller value causes splitting to occur more frequently, and *vice versa*. An intermediate value represents a compromise between too frequent splitting and no splitting at all.

Note that parcel splitting, together with their eventual removal, helps to ensure that parcels do not stay undiluted for long times. In this way, some mixing of parcel properties occurs, as would be expected at sufficiently small scales in a turbulent flow.

When a parcel is split, it is replaced by two parcels separated by a distance $d_s = (2V_i/\pi)^{1/3}$ along the direction $\boldsymbol{\omega}_i/\|\boldsymbol{\omega}_i\|$ of the original parcel's vorticity vector. The formula for d_s comes from imagining that the original "stretched" parcel has the shape of a cylinder of radius R and length $4R$; this is then split into two adjacent cylinders separated by $d_s = 2R$ centre to centre. More generally, it is consistent to take $d_s/R \propto \gamma_{\max}$. However, the precise details do not matter; up to 50% variations in d_s have no appreciable impact on the early to intermediate time flow evolution. If the z coordinate of any new parcel lies below $z = 0$ or above L_z, it is placed back on the respective boundary.

A more robust model of stretching and splitting would allow each parcel to change shape, e.g. deform as an ellipsoid (McKiver and Dritschel, 2003), in response to the local strain tensor $\boldsymbol{\nabla}\mathbf{u}$. While more physically based, this model would require tracking five additional variables, and has not been implemented for simplicity. Future work will examine its feasibility.

Over the course of a simulation, typically parcels continue to stretch and split, and thereby shrink in volume. When the volume $V_i < V_{\min}$, the parcel is mixed into the surroundings and removed from the list of parcels. Here, we use $V_{\min} = \Delta V/6^3$ by default, but again the numerical results are not strongly sensitive to this choice (section 4 below). The idea behind this parameter setting is to allow for some subgrid-scale representation, but to limit the scale separation of the smallest parcel and the advecting velocity field. The parcel motion is mainly controlled by velocity field variations at larger scales, but this cannot be expected to hold for a wide scale separation. As discussed at the beginning of this section, a similar consideration applies in two-dimensional flows, where the scale separation can be much larger (up to a

factor of 16) owing to the greater regularity of the advecting velocity field (Dritschel and Ambaum, 1997; Fontane and Dritschel, 2009).

To maintain global conservation after mixing, the volumes V_i and volume-integrated properties $b_{li}V_i$, q_iV_i and $\boldsymbol{\omega}_iV_i$ of all parcels to be removed are spread to the corners of the grid boxes they lie in, forming gridded residual fields. (In this subsection, we again use a subscript i to denote a parcel quantity and an overbar to denote a gridded field for clarity.) For example, at each grid point $\bar{\mathbf{x}}$ the residual volume $\bar{V}_{\mathrm{res}}$ and the residual volume-integrated specific humidity $\bar{Q}_{\mathrm{res}}$ are given by

$$\bar{V}_{\mathrm{res}}(\bar{\mathbf{x}}, t) = \sum_{i \in \mathcal{P}_{\mathrm{res}}(\bar{\mathbf{x}})} \phi(\mathbf{x}_i - \bar{\mathbf{x}})V_i, \tag{21}$$

$$\bar{Q}_{\mathrm{res}}(\bar{\mathbf{x}}, t) = \sum_{i \in \mathcal{P}_{\mathrm{res}}(\bar{\mathbf{x}})} \phi(\mathbf{x}_i - \bar{\mathbf{x}})q_iV_i, \tag{22}$$

where $\mathcal{P}_{\mathrm{res}}(\bar{\mathbf{x}})$ is the set of all parcels to be removed (if any) within the eight grid boxes surrounding $\bar{\mathbf{x}}$. (At the boundaries, where there are only four grid boxes above or below $\bar{\mathbf{x}}$, both $\bar{V}_{\mathrm{res}}$ and $\bar{Q}_{\mathrm{res}}$ are doubled for consistency.)

Likewise we can define analogous quantities for the original parcels to be retained:

$$\bar{V}_{\mathrm{ori}}(\bar{\mathbf{x}}, t) = \sum_{i \in \mathcal{P}(\bar{\mathbf{x}})} \phi(\mathbf{x}_i - \bar{\mathbf{x}})V_i, \tag{23}$$

$$\bar{Q}_{\mathrm{ori}}(\bar{\mathbf{x}}, t) = \sum_{i \in \mathcal{P}(\bar{\mathbf{x}})} \phi(\mathbf{x}_i - \bar{\mathbf{x}})q_iV_i, \tag{24}$$

where $\mathcal{P}(\bar{\mathbf{x}})$ is the set of all parcels to be retained within the eight grid boxes surrounding $\bar{\mathbf{x}}$ (with doubled values of $\bar{V}_{\mathrm{ori}}$ and $\bar{Q}_{\mathrm{ori}}$ at the boundaries). The sums of these quantities, $\bar{V}_{\mathrm{ori}} + \bar{V}_{\mathrm{res}}$ and $\bar{Q}_{\mathrm{ori}} + \bar{Q}_{\mathrm{res}}$, respectively equal $\bar{V}$ and $\bar{Q}$ before any parcels are removed.

The aim is to use $\bar{V}_{\mathrm{res}}$ and $\bar{Q}_{\mathrm{res}}$ to adjust V_i and q_i so that

- the sums of V_i and of Q_i over all parcels equate to the original sums before any parcels were removed, and
- the sums of $\bar{V}$ and $\bar{Q}$ over all grid points also equate to the original, and same, sums.

This adjustment can in fact be done in many ways. Here, we adjust volumes and properties *in proportion to* the original parcel volume V_i. This means that all parcels grow by the same fraction (for reasons mentioned below). To ensure global conservation, we must then divide $\bar{V}_{\mathrm{res}}$ and $\bar{Q}_{\mathrm{res}}$ by $\bar{V}_{\mathrm{ori}}$ before interpolating the residuals to the parcel positions. As a result, the new parcel volume and specific humidity are obtained from

$$V_i^{\mathrm{new}} = V_i + \sum_{\bar{\mathbf{x}} \in \mathcal{G}_i} \frac{\bar{V}_{\mathrm{res}}(\bar{\mathbf{x}}, t)}{\bar{V}_{\mathrm{ori}}(\bar{\mathbf{x}}, t)} \phi(\mathbf{x}_i - \bar{\mathbf{x}})V_i, \tag{25}$$

$$q_i^{\mathrm{new}} V_i^{\mathrm{new}} = q_iV_i + \sum_{\bar{\mathbf{x}} \in \mathcal{G}_i} \frac{\bar{Q}_{\mathrm{res}}(\bar{\mathbf{x}}, t)}{\bar{V}_{\mathrm{ori}}(\bar{\mathbf{x}}, t)} \phi(\mathbf{x}_i - \bar{\mathbf{x}})V_i, \tag{26}$$

where $\mathcal{G}_i$ is the set of all eight grid points at the corners of the grid box containing parcel i. By direct calculation, the total

volume is equal to

$$
\begin{aligned}
\sum_i V_i^{\text{new}} &= \sum_i V_i + \sum_i \sum_{\bar{\mathbf{x}} \in \mathcal{G}_i} \frac{\bar{V}_{\text{res}}(\bar{\mathbf{x}}, t)}{\bar{V}_{\text{ori}}(\bar{\mathbf{x}}, t)} \phi(\mathbf{x}_i - \bar{\mathbf{x}}) V_i \\
&= \sum_i V_i + \sum_{\bar{\mathbf{x}}} \frac{\bar{V}_{\text{res}}(\bar{\mathbf{x}}, t)}{\bar{V}_{\text{ori}}(\bar{\mathbf{x}}, t)} \sum_{i \in \mathcal{P}(\bar{\mathbf{x}})} \phi(\mathbf{x}_i - \bar{\mathbf{x}}) V_i \\
&= \sum_{\bar{\mathbf{x}}} \bar{V}_{\text{ori}}(\bar{\mathbf{x}}, t) + \sum_{\bar{\mathbf{x}}} \bar{V}_{\text{res}}(\bar{\mathbf{x}}, t) = \sum_{\bar{\mathbf{x}}} \bar{V}(\bar{\mathbf{x}}, t),
\end{aligned}
$$

where the sum over i includes all retained parcels while the sum over $\bar{\mathbf{x}}$ includes all grid points. Here we have used Equation 13 to express the final sum in the second line as $\bar{V}_{\text{ori}}$. Hence, sums over parcels equate to sums over grid points. Similarly, the total volume-integrated specific humidity is conserved; defining $Q_i \equiv q_i V_i$, we have

$$
\begin{aligned}
\sum_i Q_i^{\text{new}} &= \sum_i Q_i + \sum_i \sum_{\bar{\mathbf{x}} \in \mathcal{G}_i} \frac{\bar{Q}_{\text{res}}(\bar{\mathbf{x}}, t)}{\bar{V}_{\text{ori}}(\bar{\mathbf{x}}, t)} \phi(\mathbf{x}_i - \bar{\mathbf{x}}) V_i \\
&= \sum_i Q_i + \sum_{\bar{\mathbf{x}}} \frac{\bar{Q}_{\text{res}}(\bar{\mathbf{x}}, t)}{\bar{V}_{\text{ori}}(\bar{\mathbf{x}}, t)} \sum_{i \in \mathcal{P}(\bar{\mathbf{x}})} \phi(\mathbf{x}_i - \bar{\mathbf{x}}) V_i \\
&= \sum_{\bar{\mathbf{x}}} \bar{Q}_{\text{ori}}(\bar{\mathbf{x}}, t) + \sum_{\bar{\mathbf{x}}} \bar{Q}_{\text{res}}(\bar{\mathbf{x}}, t) = \sum_{\bar{\mathbf{x}}} \bar{Q}(\bar{\mathbf{x}}, t).
\end{aligned}
$$

Indeed, all volume-integrated parcel properties are conserved.

Splitting and mixing are carried out at the end of every time step. At this stage, we also ensure that no grid box has fewer than a specified minimum number of parcels, n_{min} (default: 3), in order to ensure $\bar{V}_{\text{ori}}(\bar{\mathbf{x}}, t) > 0$ at each grid point $\bar{\mathbf{x}}$. If fewer parcels are found, a single new parcel with volume $V_i = 2V_{\text{min}}$ is created at the centre of the grid box. To maintain conservation, a fraction f_V of the volumes $\bar{V}_{\text{ori}}(\bar{\mathbf{x}}, t)$ of the eight grid points at the corners of the grid box (in the set $\mathcal{G}_i$) is removed by creating residual volumes $\bar{V}_{\text{res}}(\bar{\mathbf{x}}, t)$ (see below). The fraction f_V is given by

$$
f_V = 2V_{\text{min}} \Big/ \sum_{\bar{\mathbf{x}} \in \mathcal{G}_i} \bar{V}_{\text{ori}}(\bar{\mathbf{x}}, t). \tag{27}
$$

Note that it is essential here to use the volume $\bar{V}_{\text{ori}}$ associated with the parcels to be retained. The new parcel is also assigned average properties found from the eight grid points. For example, the parcel specific humidity is set to

$$
q_i = \sum_{\bar{\mathbf{x}} \in \mathcal{G}_i} \bar{Q}_{\text{ori}}(\bar{\mathbf{x}}, t) \Big/ \sum_{\bar{\mathbf{x}} \in \mathcal{G}_i} \bar{V}_{\text{ori}}(\bar{\mathbf{x}}, t). \tag{28}
$$

For consistency, we must reduce $\bar{Q}(\bar{\mathbf{x}}, t)$ (and all other properties) by the same fraction f_V. This is simply accomplished by subtracting $f_V \bar{Q}_{\text{ori}}(\bar{\mathbf{x}}, t)$, for all $\bar{\mathbf{x}} \in \mathcal{G}_i$, from the residual field $\bar{Q}_{\text{res}}(\bar{\mathbf{x}}, t)$, initially zero at all grid points. The exact same operation is done for all properties, including volume. Hence, after all new parcels have been added (if any), the residual fields may contain (negative) volume and other volume-integrated properties which exactly compensate for the parcel properties assigned.

Subsequently, we add the contributions of any parcels to be removed, as in Equations 21 and 22, and update the remaining parcels as in Equations 25 and 26, excluding any new parcels

created in grid boxes with too few parcels. The properties of these new parcels are left unchanged. This is necessary to ensure exact global conservation.

Although not implemented in the present algorithm, it is possible to use the same procedure above to correct for errors in volume conservation. Parcel advection does not ensure incompressibility except in the limit of an infinite number of parcels. To correct for this, we could determine a volume residue as above, but this time defined to be equal to the difference between the grid box volume and the computed parcel interpolated volume, $\Delta V - \bar{V}(\bar{\mathbf{x}}, t)$. This residue can then be interpolated back to the parcels to dilate their volumes, adjusting other parcel properties to ensure that all volume-integrated properties remain unchanged. However, the numerical tests presented in section 4 indicate that errors in volume conservation are small at least over the time-scale of cloud development.

3.6 | Time stepping

The time evolution is carried out using a fourth-order Runge–Kutta method with an adaptive time step of length Δt. At the beginning of each time step, the maximum grid vorticity $\|\boldsymbol{\omega}\|_{\text{max}}$ is calculated and Δt is set to $\min(0.5/\|\boldsymbol{\omega}\|_{\text{max}}, \Delta t_{\text{max}})$ where Δt_{max} is typically chosen to be a quarter of the time interval between data saves. Notably, there is no CFL condition. The time step is chosen entirely for accuracy, and can be significantly larger than required in grid-based models at high resolution. We have verified that reducing Δt by a factor of 2 has a negligible impact on the results at early to intermediate times (section 4 below); at later times, errors amplify significantly, as expected in a turbulent flow. Note that any other time-stepping method could have been used.

A schematic of the procedures comprising the MPIC algorithm is provided in Figure 1.

4 | NUMERICAL TESTS AND PARAMETER SETTINGS

We next examine the behaviour of the new MPIC model, in particular its dependence on numerical parameter settings, and illustrate how well the model compares with a state-of-the-art conventional numerical model (the focus of Böing *et al.*, forthcoming). For this purpose, we study the evolution of a moist, initially buoyant thermal located near the ground level. The thermal rises at first through a neutrally stable lower atmospheric layer before encountering a stable layer aloft. The initial fields of buoyancy $b = b_l$ and fractional specific humidity $\tilde{q} = q/q_0$ are shown in Figure 2 together with a schematic of the background environment. Condensation (cloud formation) occurs once the thermal rises past the lifting condensation level $z = z_c$. The condensation releases additional buoyancy, thereby increasing the vertical
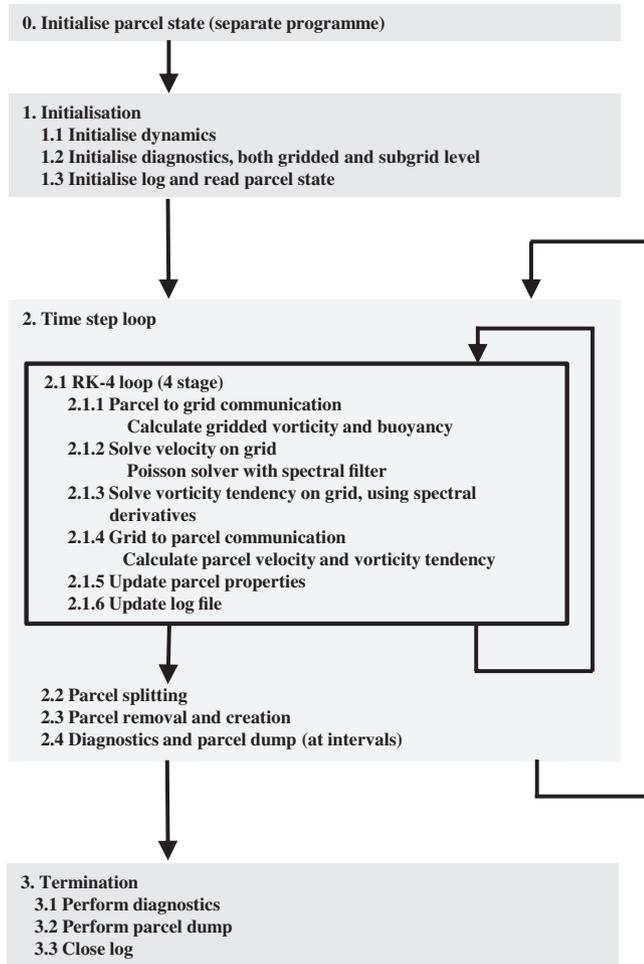
FIGURE 1 A flow chart of the MPIC algorithm

acceleration, and takes the thermal past its level of dry neutral buoyancy $z = z_d$. Only when the thermal encounters the level of moist neutral buoyancy $z = z_m$ (the nominal cloud top) is the upward acceleration arrested. All these heights are defined in terms of a non-mixing parcel which does not overshoot its height of neutral buoyancy. Throughout the evolution of the thermal, significant turbulent entrainment occurs (see below), so in fact only part of the thermal actually rises this far. The remainder becomes increasingly well mixed with the surrounding environment.

4.1 | Non-dimensionalization

For convenience, we scale all variables in order to work with the fewest parameter combinations possible. Lengths are made dimensionless by taking the condensational scale height $1/\lambda = 1$ in Equation 5. Time is made dimensionless by taking the characteristic squared buoyancy frequency $g\lambda\Delta\theta_{l0}/\theta_{l0} = 1$, where $\Delta\theta_{l0}/\theta_{l0} = 0.01$ is a characteristic fractional variation of the liquid-water potential temperature. This gives a dimensionless gravity of $g = 100$. We scale the specific humidity q by its saturation value q_0 at ground level (i.e. we use $\widetilde{q} = q/q_0$ in what follows), in terms of which we obtain the following dimensionless expression for

the buoyancy b:

$$b = b_l + b_m \max\left(0, \widetilde{q} - e^{-z}\right),\tag{29}$$

where

$$b_m = \frac{gLq_0}{c_p\theta_{l0}}.\tag{30}$$

Here, we take $L/c_p = 2,500\,\mathrm{K}$, $q_0 = 0.015$ and $\theta_{l0} = 300\,\mathrm{K}$. This gives $b_m = 12.5$. In terms of the original, dimensional value of gravity g, the buoyancy b is scaled by the characteristic value $g\Delta\theta_{l0}/\theta_{l0}$, which is here 1% of g.

4.2 | Initialization

At the initial time $t = 0$, we place a spherical thermal of weakly varying liquid-water buoyancy b_l and uniform (fractional) specific humidity $\widetilde{q} = \widetilde{q}_{th}$ adjacent to the ground $z = 0$. The thermal has radius R and is centred at $\mathsf{x} = (L_x/2, L_y/2, R)$. To create an asymmetry in the subsequent evolution, we take b_l of the form

$$b_l = b_{l\,th}\left(1 + \frac{e_1 x'y' + e_2 x'z' + e_3 y'z'}{R^2}\right),\tag{31}$$

where $x' = x - L_x/2$, $y' = y - L_y/2$ and $z' = z - R$, while e_1, e_2 and e_3 are dimensionless constants. This preserves the mean value of b_l as well as the centre of mass of the perturbation.

The environment around the thermal extending to the base of the stratified zone at $z = z_b$ is assumed to be well mixed, with $b_l = 0$ (without loss of generality) and having a uniform specific humidity $\widetilde{q}_{env}$ a factor of μ times that in the thermal, $\widetilde{q}_{th}$. We specify the lifting condensation level z_c, from which we obtain the specific humidity within the thermal: $\widetilde{q}_{th} = \exp(-z_c)$. In turn, given μ, we obtain the specific humidity in the environment around the thermal: $\widetilde{q}_{env} = \mu\widetilde{q}_{th}$.

Next we specify the relative humidity $h = h_b$ at $z = z_b$. This, together with the environmental specific humidity, determines z_b through $z_b = \ln(h_b/\widetilde{q}_{env})$. Finally, we specify two further heights, the level of dry neutral stratification z_d for the thermal, and the level of moist neutral stratification (the nominal cloud top) z_m. From these values, we obtain the thermal buoyancy

$$b_{l\,th} = N^2(z_d - z_b), \qquad \text{where } N^2 = b_m\frac{e^{-z_c} - e^{-z_m}}{z_m - z_d}\tag{32}$$

is the squared buoyancy frequency in the stratified zone. This follows from the requirements that (a) the thermal buoyancy matches the background stratification at $z = z_d$ (normally near or just above the condensation level z_c), and (b) the total buoyancy at cloud top $z = z_m$ matches the background stratification, i.e.

$$b_{l\,th} + b_m\left(\widetilde{q} - e^{-z_m}\right) = N^2(z_m - z_d).\tag{33}$$

The idea is that the thermal rises through the condensation level before its upward motion is inhibited at the level of dry neutral stratification. Condensation will release buoyancy, causing the thermal to accelerate until it reaches the nominal cloud-top level.
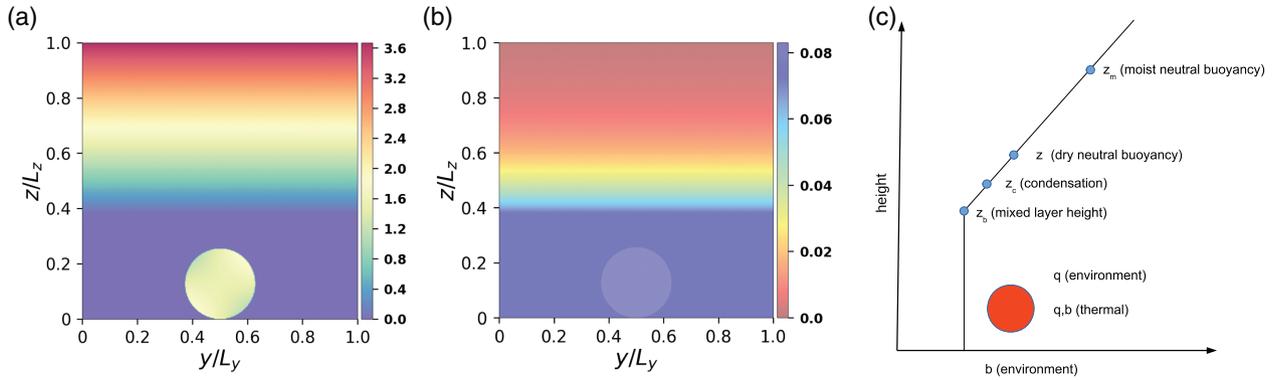
FIGURE 2 Initial distributions of (a) liquid water buoyancy b_l and (b) specific humidity fraction $\widetilde{q}$ in a vertical cross-section cutting through the initial thermal. The basic-state stratification profile is shown in (c)

TABLE 1 List of physical parameters used in the simulations conducted. Units are included for dimensional quantities; all other quantities are dimensionless

Physical parameter	Value	Comment
Mean liquid water potential temperature θ_{l0} (K)	300	Default
Characteristic variation of θ_{l0}, $\Delta\theta_{l0}/\theta_{l0}$	0.01	Default
Non-dimensional condensational scale height $1/\lambda$	1.0	Default
Non-dimensional squared buoyancy frequency $g\lambda\Delta\theta_{l0}/\theta_{l0}$	1.0	Default
Saturation specific humidity q_0 at ground level	0.015	Default
Scaled latent heat L/c_p (K)	2500	Default
Relative humidity $h = h_b$ at $z = z_b$	0.8	Chosen
Condensation level z_c	2.5	Chosen
Specific humidity ratio $\mu = \widetilde{q}_{env}/\widetilde{q}_{th}$	0.9	Chosen
Level of dry neutral stratification z_d	4.0	Chosen
Level of moist neutral stratification z_m	5.0	Chosen
Radius of spherical thermal R	0.8	Chosen
Thermal buoyancy asymmetry factors e_1, e_2 and e_3	0.3, −0.4, 0.5	Chosen
Specific humidity fraction inside thermal $\widetilde{q}_{th}$	0.08208	Derived
Specific humidity fraction outside thermal $\widetilde{q}_{env}$	0.07388	Derived
Height of the top of the mixed layer z_b	2.38222	Derived
Buoyancy frequency N in the stratified zone	0.97048	Derived
Thermal liquid water buoyancy b_{lth}	1.52369	Derived
Thermal fractional potential temperature anomaly $(\theta_{th} - \theta_{l0})/\theta_{l0}$	0.01524	Derived
Latent buoyancy $b_m = gLq_0/(c_p\theta_{l0})$	12.5	Derived

A full list of parameters used for the experiment conducted is provided in Table 1.

4.3 | Default numerical parameter settings

For testing purposes, we consider a computational domain having side lengths $L_x = L_y = 2\pi$ and a specified height L_z (here also 2π). This is large enough to accommodate the condensational scale height $1/\lambda$, here unity. The upper boundary has only a small influence until late times, $t > 10$. The domain is divided into equal-sized grid boxes, with side lengths $\Delta x = L_x/n_x$, $\Delta y = L_y/n_y$ and $\Delta z = L_z/n_z$. Here, with $L_x = L_y = L_z$ we use an isotropic grid with $n_x = n_y = n_z = n_g$, and choose $n_g = 128$ as the default; other values are discussed below and in Böing *et al.* (forthcoming). As discussed at the end of section 3, the time step Δt is adapted every

time step to be inversely proportional to the maximum vorticity magnitude, i.e. $\Delta t = 0.5/\|\omega\|_{max}$. This relationship is justified below by comparing both smaller and larger time steps (varying the prefactor 0.5 above). The only remaining numerical parameters are the dimensionless maximum parcel stretch γ_{max} (default 4) and the minimum parcel volume fraction $\widehat{V}_{min} = V_{min}/\Delta V$ (default $1/6^3$). Below, we discuss the impact of varying these parameters about their default values.

4.4 | Description of the flow evolution

To set the stage, we begin with a qualitative description of the flow evolution as obtained using the default numerical parameter settings. Images are rendered on a grid four times

finer in each direction than the basic "inversion" grid (n_g^3). In fact any grid resolution could be used for the rendering, since the parcels alone determine the field values but, given our choice of the minimum parcel size, any finer rendering grid would produce a grainy appearance. Details of the rendering procedure may be found in Böing *et al.* (forthcoming).

Figure 3 illustrates a few stages in the flow evolution. Here we show the total buoyancy b, specific humidity $\widetilde{q}$, condensed portion $\widetilde{q}_c$ of $\widetilde{q}$ (cloud amount), and the parcel vorticity magnitude $\|\boldsymbol{\omega}\|$, all in a vertical cross-section $x = L_x/2$ slicing through the centre of the thermal initially (other views are similar). The parcel vorticity is shown in place of the total vorticity since the former can be obtained directly on a fine grid from the parcels and, moreover, dominates the residual correction required to make the total vorticity solenoidal. The results shown compare closely with those obtained using the Met Office/NERC cloud model (MONC) run at more than double resolution (section 4.10 below and Böing *et al.*, forthcoming).

At early times, the thermal deforms into a large vortex ring, forming a strong updraught near its centre and entraining air from the sides and below. This updraught is compensated by subsidence mainly around the outskirts of the ring (not shown). By time $t = 2$, part of the thermal has pushed through the lifting condensation level at $z_c = 2.5$ (corresponding to $z/L_z \approx 0.4$ along the vertical axis) forming a small cap-like cloud. The cap-like cloud is partially environmental air that is pushed up by the actual thermal. The vorticity at this early stage is concentrated in a narrow zone near the edge of the thermal where horizontal gradients of b are largest. As time advances, the thermal becomes progressively more turbulent, entraining and mixing more low humidity air (see $\widetilde{q}_c$ at $t = 6$ in particular). The vorticity partially collapses into a ring with an intense core at $t = 4$, then subsequently destabilizes and breaks down. This generates a multitude of billowing fine-scale structures reminiscent of actual cumulus convection (e.g. $\widetilde{q}_c$ at $t = 4$ in Figure 3). This process is described in detail in Grabowski and Clark (1993). The turbulence at the edge of a real cloud as it ascends is more intense than in this simulation, but is better captured at higher resolution (sections 4.9 and 4.10 below). By time $t = 6$, part of the thermal reaches the level of moist neutral stratification $z_m = 5.0$ (corresponding to $z/L_z \approx 0.8$), where it begins to spread out and gradually dissipate. By the end of the simulation at $t = 10$, the cloud has spread across most of the horizontal domain and contains much weaker updraughts and downdraughts (not shown).

This example serves to illustrate the rapid changes occurring on small scales within clouds as a result of variations in thermodynamic properties, as mentioned above. Modelling this complexity, both accurately and efficiently, is a severe challenge for any numerical model. We next examine how robust the MPIC model is in faithfully capturing the evolution. In particular, we examine the dependence on various numerical parameters, as well as on spatial and temporal resolution.

4.5 | Dependence on maximum parcel stretch

We first examine the maximum parcel stretch γ_{max} which is used in Equation 20 to determine when a parcel should split into two. The greater the maximum parcel stretch, the longer a parcel stays intact. Here, we compare four values: $\gamma_{max} = 2$, 4 (the default), 8 and ∞ (for which splitting never occurs). In Figure 4, we qualitatively illustrate the dependence on γ_{max} by comparing cross-sections of the total buoyancy field b in each simulation, at both an intermediate and a late time ($t = 4$ and 8). All simulations are closely comparable, but the one with the smallest maximum stretch ($\gamma_{max} = 2$) exhibits the greatest differences overall. Evidently, too frequent splitting causes numerical diffusion, removing small-scale features. On the other hand, the case with no parcel splitting ($\gamma_{rmmax} = \infty$) is remarkably similar to the other two with moderate values of γ_{max}. Nonetheless, we argue that some parcel splitting is necessary to more accurately resolve small-scale features, as well as to represent the effect of small-scale mixing integrated over the time evolution of the flow.

Differences between the simulations can be seen more clearly in the kinetic energy spectrum $\mathcal{K}(k)$ and in the parcel number density $p_{vol}(\widehat{V})$, shown in Figure 5 at the same times illustrated in Figure 4. The spectrum $\mathcal{K}(k)$ is defined as the sum of $(\widehat{u}\widehat{u}^* + \widehat{v}\widehat{v}^* + \widehat{w}\widehat{w}^*)/2$ over all wavevectors $\mathbf{k}$ whose magnitude $|\mathbf{k}|$ lies between $k - 1/2$ and $k + 1/2$ ($*$ denotes complex conjugation). Also, $p_{vol}(\widehat{V})d\widehat{V}$ gives the number of parcels having a volume fraction lying between $\widehat{V}$ and $\widehat{V} + d\widehat{V}$. In practice p_{vol} is computed using finite-sized bins $\Delta\widehat{V}$ uniformly spaced in log $\widehat{V}$. In Figure 5, the case with the smallest γ_{max} (= 2, black curve) exhibits the greatest discrepancies, with noticeably less kinetic energy at small scales (high total wavenumbers k). Likewise, the case with no splitting (magenta curve) has significantly less kinetic energy at large and intermediate scales, and marginally greater kinetic energy at small scales. In the parcel number density, p_{vol}, we can see that the high maximum stretch case $\gamma_{max} = 8$ (red curve) struggles to produce small parcels. (The magenta curves remain unchanged since no parcels split in this case). The low maximum stretch case $\gamma_{max} = 2$ (black curve) produces the greatest number of parcels, particularly at small scales as expected. Note that the fluctuations seen in p_{vol} at larger volume fractions arise from splitting parcels by factors of 2 together with the low sample size. The fluctuations diminish at later times (not shown) and are also weaker at higher resolution.

Further differences are revealed by examining the evolution of global diagnostics such as field minima, maxima and r.m.s. values (these diagnostics have been computed from the gridded fields). In Figure 6, we show the time evolution of the r.m.s. velocity $u_{rms} \equiv \|\mathbf{u}\|_{rms}$, the maximum
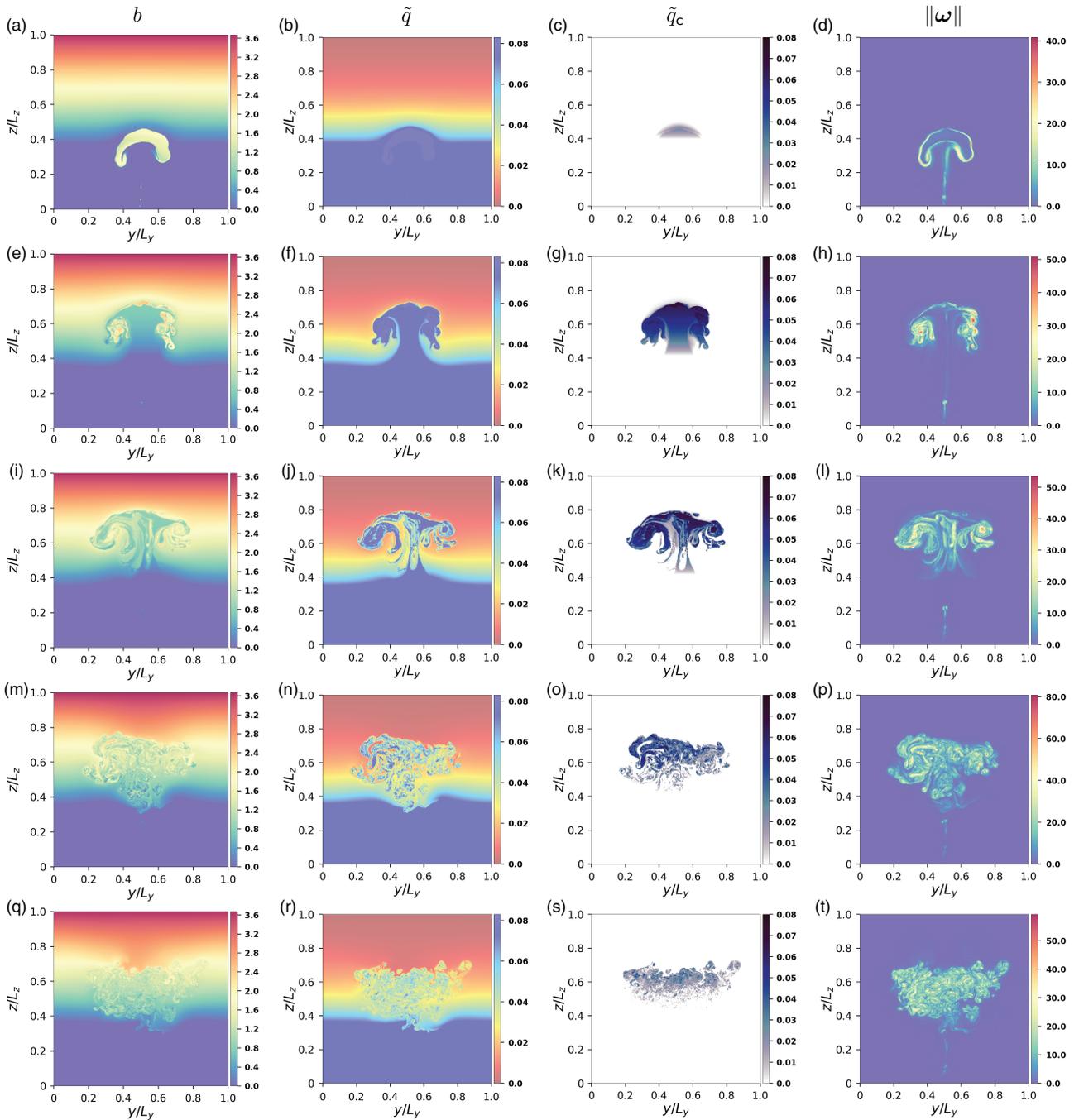
FIGURE 3 Time evolution of (a, e, i, m, q) total buoyancy b, (b, f, j, n, r) specific humidity $\tilde{q}$, (c, g, k, o, s) nominal cloud amount $\tilde{q}_c$ and (d, h, l, p, t) parcel vorticity magnitude $\|\boldsymbol{\omega}\|$. Time t increases downwards with $t =$ (a–d) 2, (e–h) 4, (i–l) 6, (m–p) 8 and (q–t) 10. The fields in this and subsequent figures are shown in a vertical cross-section cutting through the centre of the domain at $x = L_x/2$

(total) vorticity magnitude $\omega_{max} \equiv \|\boldsymbol{\omega}\|_{max}$, and the number of parcels n (with $\log_{10}$ scaling) for four values of γ_{max} (these diagnostics are representative). Here, the case with no parcel splitting (magenta curve) has significantly lower u_{rms} and relatively high ω_{max}. This is found also for the large maximum stretch case $\gamma_{max} = 8$ (red curve), albeit with a smaller discrepancy in u_{rms}. The small maximum stretch case $\gamma_{max} = 2$ (black curve) compares closely with the default case ($\gamma_{max} = 4$, blue curve) for u_{rms} but shows much lower values of ω_{max}. Collectively, these results, and others (not presented) for $\gamma_{max} = 1.5$, 3 and 6, indicate that our default

choice $\gamma_{max} = 4$ produces the least anomalous behaviour overall.

4.6 | Dependence on minimum parcel volume fraction

We next consider the effect of the smallest parcel size, specified by the minimum volume fraction $\widehat{V}_{min}$. Three values are considered in Figure 7, namely $\widehat{V}_{min} = 1/4.5^3$ (large), $1/6^3$ (medium; default), and $1/8^3$ (small). Comparisons are shown for $t = 4$ and $t = 8$ as before. Differences are slight at $t = 4$ and mainly occur at the smallest scales, which are
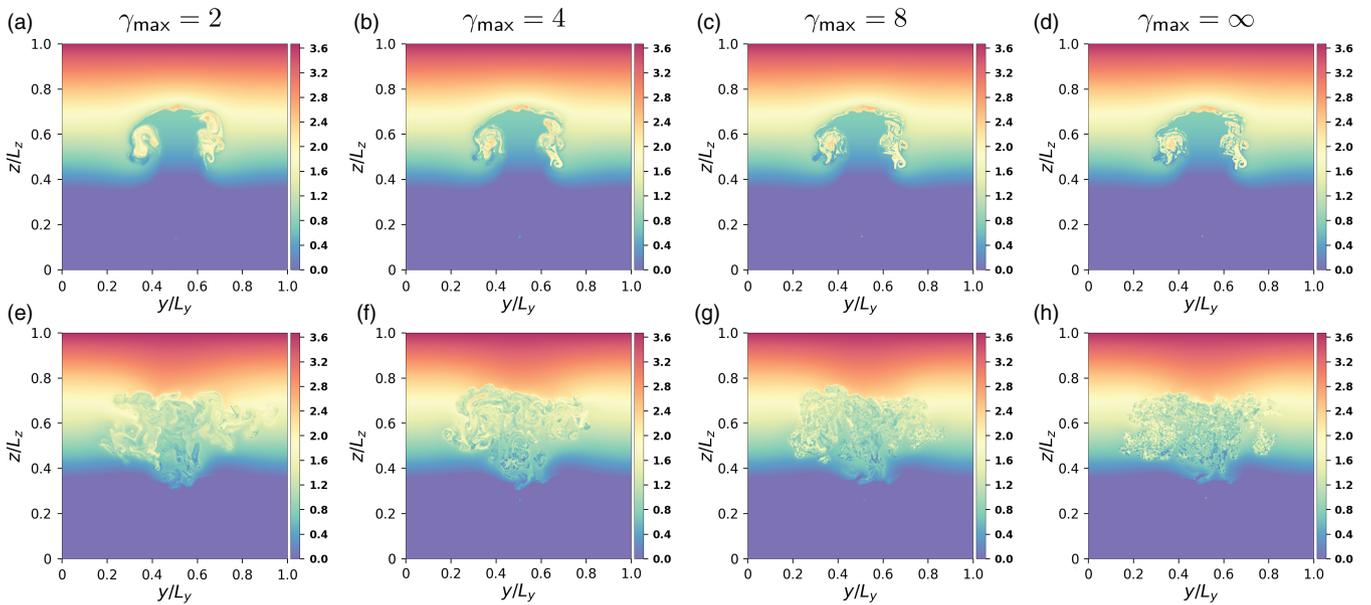
FIGURE 4 Comparison of the total buoyancy b at (a–d) $t = 4$ and (e–h) $t = 8$, for different values of the maximum parcel stretch γ_{max}: (a, e) 2, (b, f) 4, (c, g) 8 and (d, h) ∞
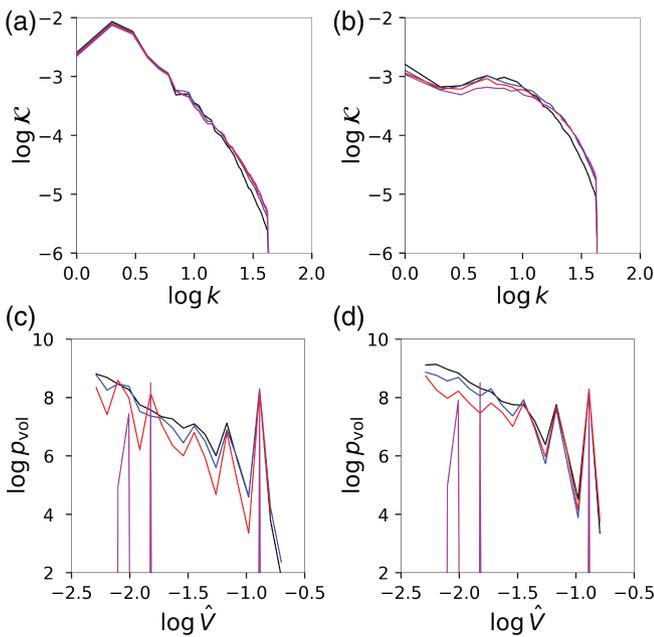
FIGURE 5 Kinetic energy spectra $\mathcal{K}(k)$ at (a) $t = 4$ and (b) $t = 8$, together with parcel number density $p_{vol}(\widehat{V})$ where $\widehat{V}$ is the parcel volume fraction at (c) $t = 4$ and (d) $t = 8$, for four different maximum stretch values: $\gamma_{max} = 2$ (black), 4 (blue), 8 (red) and ∞ (magenta). The kinetic energy spectra are computed from the velocity field on a 128^3 grid. The effect of the de-aliasing filter is seen by the sudden drop in $\mathcal{K}$ near $k = 128/3$. Here and in subsequent figures, log denotes the base 10 logarithm

least predictable. However, by $t = 8$ larger-scale differences emerge, which appear to be greater between the large and medium values of $\widehat{V}_{min}$ than between the medium and small values. *A priori* one expects the smallest $\widehat{V}_{min}$ to be most accurate, since a wider range of scales is resolved in this case. But this comes at a high computational expense (the number of parcels is proportional to $1/\widehat{V}_{min}$), and moreover there is

no explicit representation of the subgrid flow field to justify retaining parcels well below the grid size.

Global measures such as the r.m.s. velocity u_{rms} and the maximum vorticity magnitude ω_{max} confirm that the two smallest volume fractions produce the most comparable results. This is shown in Figure 8 along with the number of parcels n. The red curve in these plots corresponds to the largest minimum volume fraction. This case underestimates both u_{rms} and ω_{max}, the latter even at early times ($t > 1$). Judging from the behaviour of n, there is an excessive removal of small parcels, and these parcels typically contain the largest vorticity magnitudes. From these results, and by examining other measures such as the minimum and maximum vertical velocity, we selected $\widehat{V}_{min} = 1/6^3$ as the default value, as a compromise between accuracy and efficiency.

4.7 | Dependence on time step

In the MPIC model, the time step Δt need only be chosen for accuracy – there is no stability restriction. In this subsection we examine three choices for Δt differing by factors of two: $\Delta t = 1/\|\boldsymbol{\omega}\|_{max}, 0.5/\|\boldsymbol{\omega}\|_{max}$ (the default), and $0.25/\|\boldsymbol{\omega}\|_{max}$. The inverse scaling on maximum vorticity magnitude in the domain ensures that the most rapidly spinning motions are at least marginally resolved. We have also tested an inverse scaling on the maximum velocity gradient, which is a better measure of how rapidly parcel trajectories can change. This produces closely comparable results since in practice the maximum velocity gradient is roughly proportional to maximum vorticity magnitude. However, computing the velocity gradient requires extra computational work, so we have taken the simpler approach here.

Figure 9 compares the three time step choices, with time step decreasing from left to right, at the same two times $t = 4$
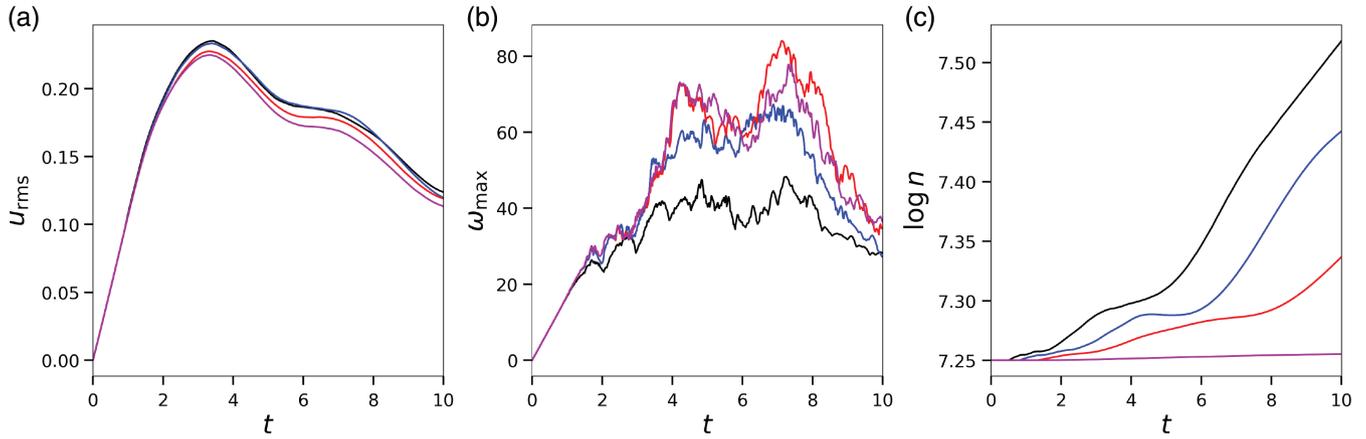
FIGURE 6 Time evolution of (a) the r.m.s. velocity, (b) the maximum vorticity magnitude and (c) the number of parcels, for four different maximum stretch values: $\gamma_{max} = 2$ (black), 4 (blue), 8 (red) and ∞ (magenta)
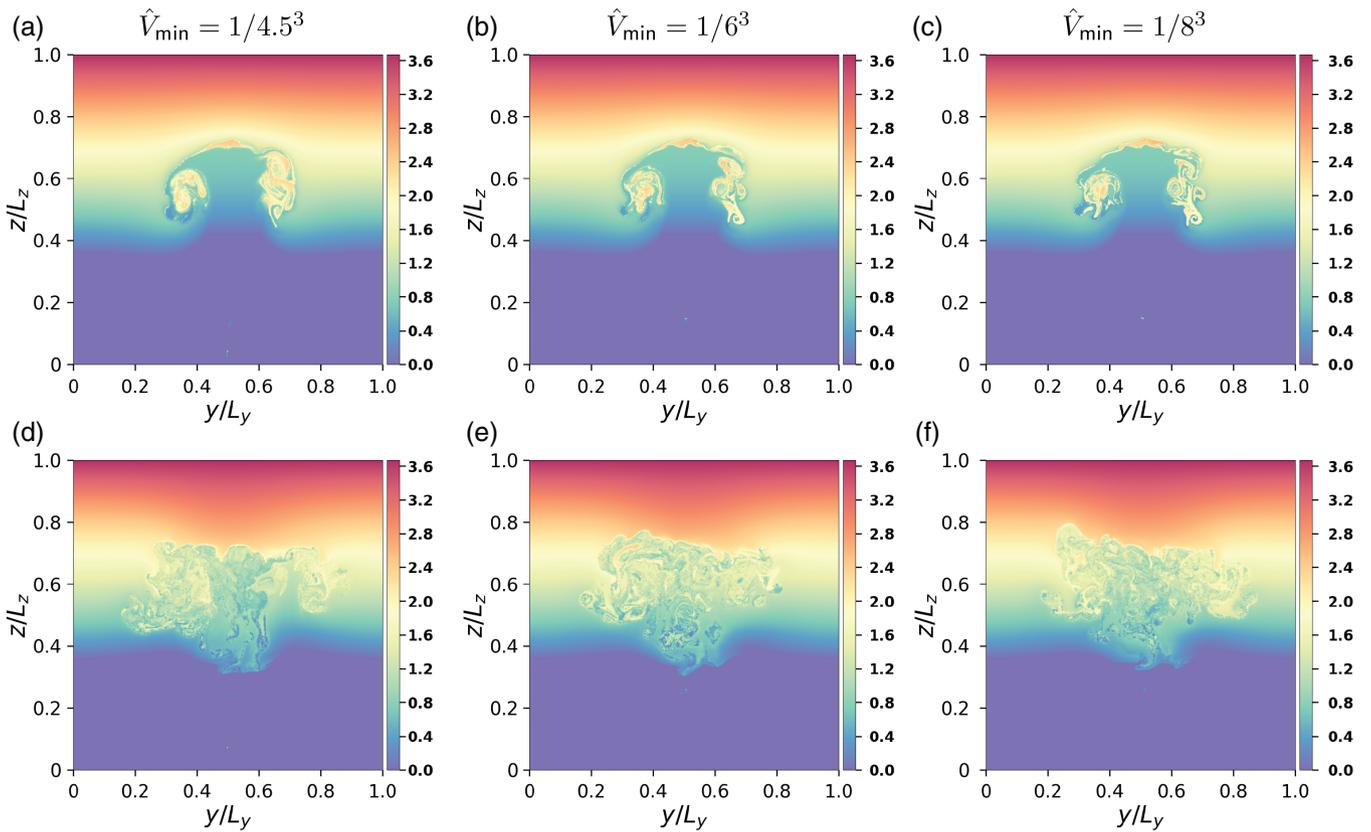
FIGURE 7 Comparison of the total buoyancy b at (a–c) $t = 4$ and (d–f) $t = 8$, for different values of the minimum parcel volume fraction $\hat{V}_{min}$: (a, d) $1/4.5^3$, (b, e) $1/6^3$ and (c, f) $1/8^3$

and 8 illustrated in the previous comparisons. At $t = 4$, differences are almost negligible. Larger differences emerge by $t = 8$, but they are generally less significant than seen either for variations in γ_{max} or $\hat{V}_{min}$ (cf. Figures 4 and 7). Again the two smallest time steps are most comparable apart from the fine details. Differences in global measures such as u_{rms} and ω_{max} are also much less significant (not shown). In short, the dependence on time step is particularly weak. We have selected $\Delta t = 0.5/\|\omega\|_{max}$ as the default setting, but if necessary a value twice this large could be used to lower computational cost with only a small loss of accuracy.

4.8 | Incompressibility

As already discussed above, parcel-based methods do not guarantee incompressibility (or mass conservation in general), in the sense of parcel volume at each grid point remaining homogeneous. Advection of a finite number of parcels inevitably leads to a discrepancy between the grid box volume ΔV and its parcel-interpolated approximation $\bar{V}(\bar{\mathbf{x}}, t)$. However, we have found that the MPIC model approximates the incompressibility constraint accurately, as shown below. This is likely due to the fact that a large number of parcels (10s
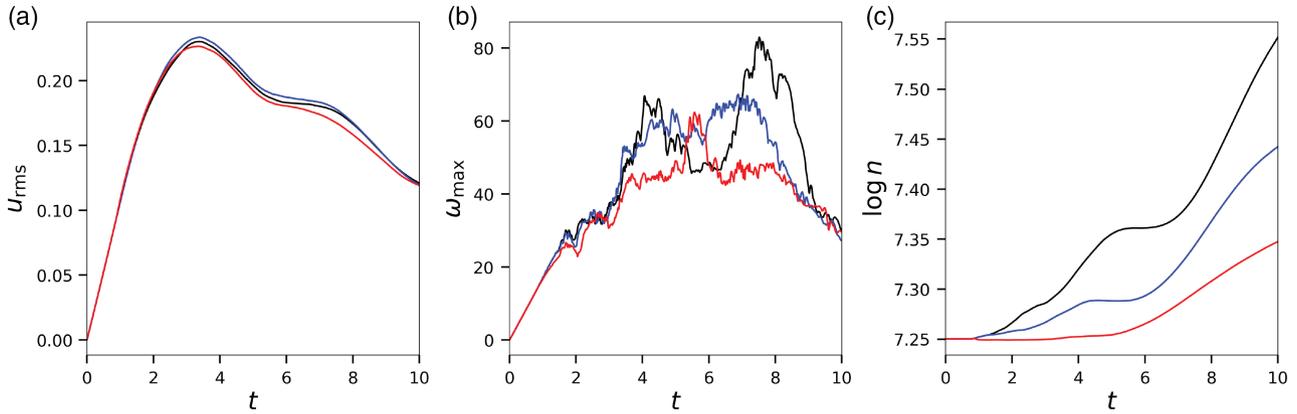
FIGURE 8 Time evolution of (a) the r.m.s. velocity, (b) the maximum vorticity magnitude and (c) the number of parcels, for three different minimum parcel volume fractions: $\hat{V}_{min} = 1/8^3$ (black), $1/6^3$ (blue) and $1/4.5^3$ (red)
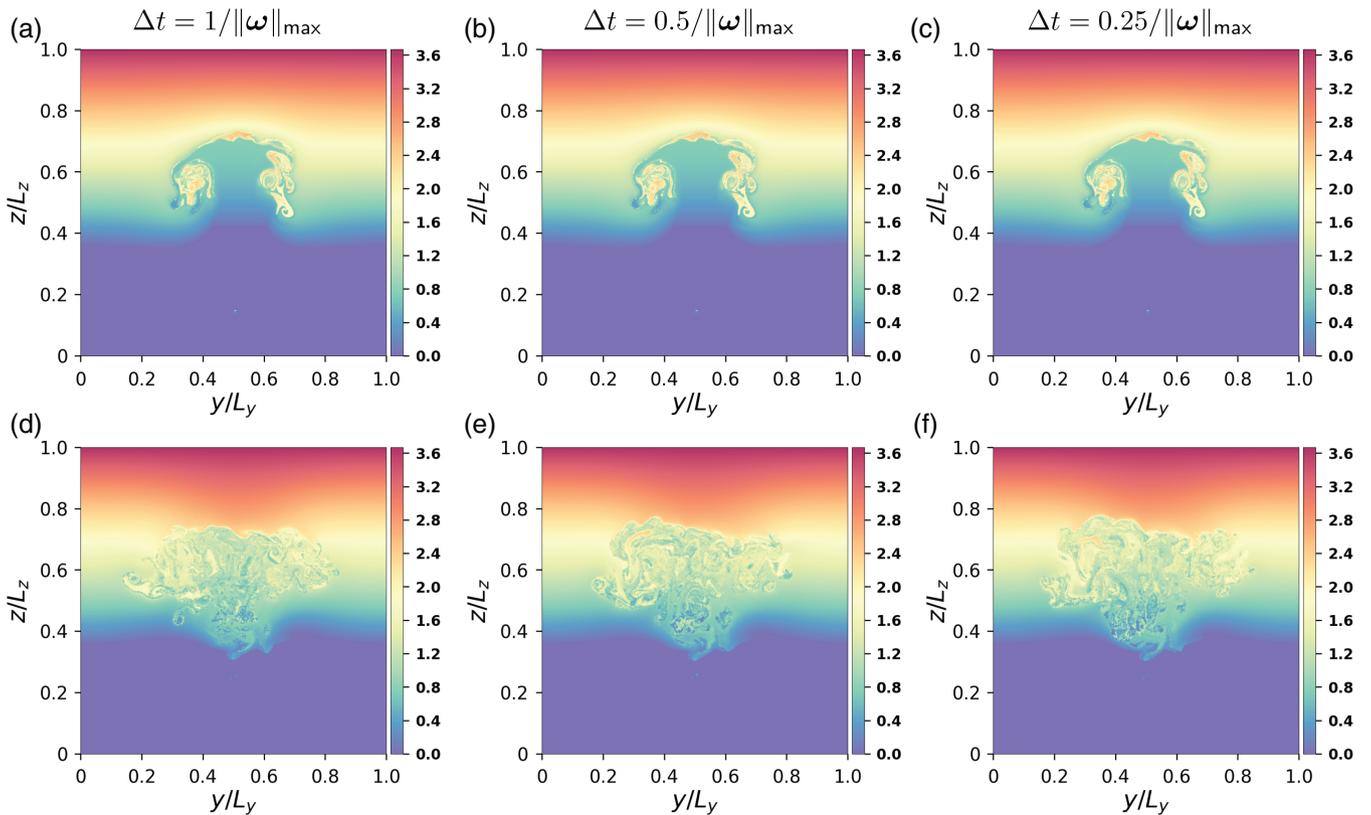
FIGURE 9 Comparison of the total buoyancy b at (a–c) $t = 4$ and (d–f) $t = 8$, for different time steps Δt: (a, d) $1/\|\boldsymbol{\omega}\|_{max}$, (b, e) $0.5/\|\boldsymbol{\omega}\|_{max}$, and (c, f) $0.25/\|\boldsymbol{\omega}\|_{max}$

to 100s) contribute to the calculation of $\bar{V}(\bar{\mathbf{x}}, t)$ at each grid point $\bar{\mathbf{x}}$.

To demonstrate this, we analysed a 256^3 simulation of the rising thermal test case at times $t = 0, 2, ..., 10$. First, we computed the standard deviation in the volume fraction

$$\sigma(\Delta z) = \sqrt{n_g^{-3} \sum_{\bar{\mathbf{x}}} \{\bar{V}(\bar{\mathbf{x}}, t)/\Delta V - 1\}^2}, \quad (34)$$

where the sum is taken over all grid points and $n_g = 256$ in this case. Here $\Delta z = L_z/n_g$ is the z grid length (recall $L_z = 2\pi$). We then performed a 1-2-1 average in each direction to obtain $\bar{V}$ on a grid twice as coarse, then repeated the above calculation for the variance (in which Δz

is doubled). We continued averaging to successively coarser grids until we reached a 4^3 grid, thereby calculating the variance $\sigma(\Delta z)$ as a function of scale Δz. In this way, we gain an understanding of how errors in volume conservation depend on scale.

The results are shown in Figure 10 in log–log scaling, for all six times analysed. First, the error grows in time, though it rapidly saturates. Second, the error is small: less than 5% for the variance at the smallest scale and at the latest time. Hence, over the lifetime of cloud development in this test case, the errors in incompressibility are small. For much longer simulations, it may be necessary to correct this error. This would
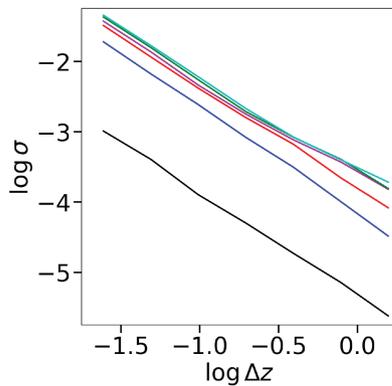
FIGURE 10 Volume fraction variance σ versus grid scale Δz (or scale of averaging) at times $t = 0$ (black), 2 (blue), 4 (red), 6 (magenta), 8 (green) and 10 (cyan)

require a minor modification of the numerical method, as discussed above in section 3.5, and will be implemented only if the errors at long times prove significant.

4.9 | Dependence on resolution

Finally, we examine the dependence on resolution n_g. This has by far the greatest impact among all parameter variations considered. But increasing resolution also has the highest price tag; it is not something that can be done indefinitely.

Ideally, one would hope that the results converge with increasing resolution, but this is unlikely in the present model framework. Each increase in resolution activates new and intense motions, particularly in vorticity, leading to stronger turbulence, and thereby greater entrainment and mixing. In fact, one can only hope for convergence at the large to intermediate scales, and expect the loss in predictability to move upscale as time advances. This is because the scales of motion below any fixed scale do eventually impact those above it, due to nonlinear interactions. The importance of those interactions controls the predictability time of any given scale.

Figure 11 shows the total buoyancy field b simulated at three resolutions, increasing by factors of 2 (in each coordinate direction) from left to right, with the 128^3 case previously illustrated shown in the middle. Here, times $t = 2$, 4, 6 and 8 are compared. At all times, there is a substantial increase in complexity of the flow field with resolution. Moreover, the small-scale structures grow in intensity, predominantly in the vorticity field (see below). At the earliest time shown, $t = 2$, the large-scale features are captured at all resolutions, with the agreement between each increase in resolution improving and extending to smaller scales. This is not immediately obvious in this visual comparison because we are not comparing images filtered to the same resolution. But convergence is seen in the kinetic energy spectra $\mathcal{K}$ shown in Figure 12, which includes a lower-resolution case with $n_g = 32$. At the earliest time shown, $t = 2$, the spectra compare well across all commonly resolved scales. Then, as time advances,

predictability is lost for progressively larger scales. In the spectra, this is seen by the splaying apart of the various curves for different resolutions. The agreement between the spectra erodes in time, though as expected the two highest resolutions show the closest agreement over the largest range of scales for the longest times.

At the highest resolution, the rapid crinkling of the buoyancy field b is due to the generation of intense vortical structures on the sharp interface between the thermal and the surrounding environment as the thermal rises. With increasing resolution, the crinkling occurs on smaller scales at a faster rate. This is limited ultimately by diffusion at scales well beyond the reach of any current numerical model. Despite this lack of convergence at small to intermediate scales, the large-scale structure of the rising thermal is captured at all resolutions, though more realistically at higher resolution.

The convergence with resolution can also be seen in the global measures such as $u_{\rm rms}$ and $\omega_{\rm max}$ shown in Figure 13 together with the total number of parcels n. In $u_{\rm rms}$, a measure of the kinetic energy content of the flow, the two highest resolutions $n_g = 128$ and 256 (red and magenta curves) remain closest for longest, and only depart significantly by around $t = 5$. At progressively lower resolution, the curves depart more strongly and at earlier times from the highest-resolution results for $u_{\rm rms}$. On the other hand, there is no convergence for the maximum vorticity $\omega_{\rm max}$. Each doubling in resolution doubles $\omega_{\rm max}$ at early times. This is simply a consequence of the fact that vorticity is generated by horizontal gradients in buoyancy, and the initial buoyancy is not continuous across the thermal boundary. Thus, the maximum *numerical* buoyancy gradient is inversely proportional to the horizontal grid spacing, i.e. proportional to n_g. Nonetheless this very large variation in $\omega_{\rm max}$ has little impact on $u_{\rm rms}$, which is an integrated measure of the vorticity throughout the domain. That is, high localized vorticity values do not appreciably impact the velocity field, in an average r.m.s. sense. Finally, the number of parcels n increases in proportion to the total number of grid boxes n_g^3, since the number of parcels per grid box is roughly the same in all cases.

While the resolutions examined here are modest, they are high compared to what can be presently afforded by GCMs and even cloud-permitting models on a global domain. If MPIC can still resolve general aspects of moist processes at very coarse resolutions, then MPIC would offer a potentially significant improvement in modelling such processes. To examine this, we consider three coarser resolutions, $n_g = 8$, 16 and 32. When $n_g = 8$, the grid length is equal to the radius of the thermal. Figure 14 compares the total buoyancy field b at these three resolutions, at times $t = 2$, 4, 6 and 8. The higher resolution results may be found in Figure 11 for comparison. Remarkably, broad features of the evolution are still captured at these resolutions, with only the coarsest resolution standing out to some extent. At this resolution, the thermal development is a little delayed, yet at later times a
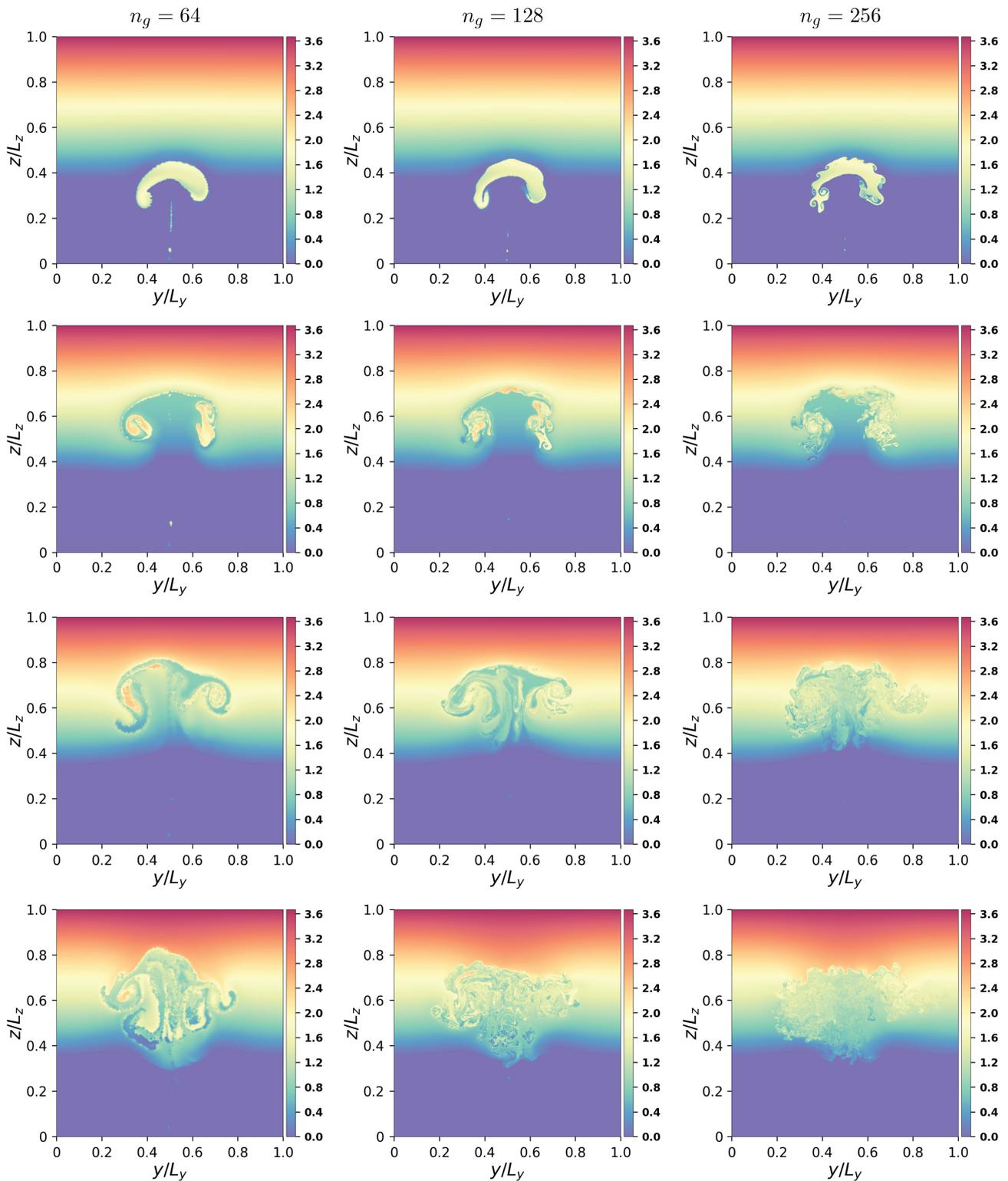
FIGURE 11 Comparison of the total buoyancy b at t = (a–c) 2, (d–f) 4, (g–i) 6, and (j–l) 8, for resolutions n_g = (a, d, g, j) 64, (b, e, h, k) 128 and (c, f, i, l) 256

similar amount of condensation occurs (see below). Despite the very poor resolution, MPIC still manages to resolve moist convection *without any parametrizations*. The key advantage of MPIC is the *explicit* representation of sub-grid processes via parcels.

We conclude this comparison across resolution by an examination of the nominal cloud amount $\widetilde{q}_c$, shown in Figure 15 at two times, first when the cloud is at its most developed

stage ($t = 6$), and second when the cloud has begun to decay ($t = 8$). Here, resolutions n_g = 64, 128 and 256 are compared. While the lower resolution captures only gross features, the two higher resolutions begin to exhibit billowing fine-scale structures observed in real cumulus convection. These images provide a glimpse into the detail which may be captured by the MPIC model at yet higher resolution. Such detail is likely to be important for entrainment and mixing, and as such the
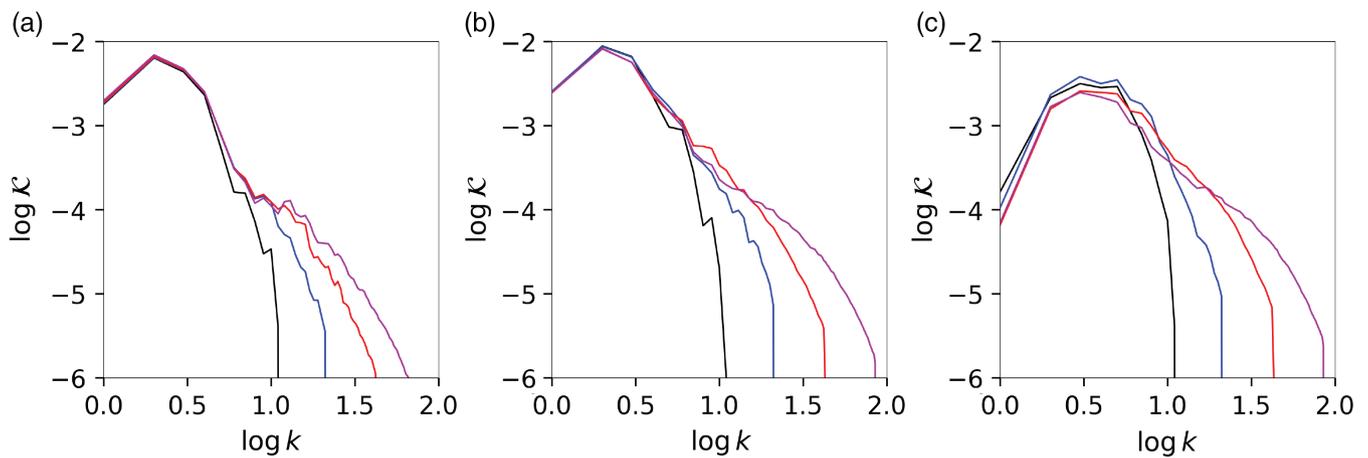
FIGURE 12   Kinetic energy spectra $\mathcal{K}(k)$ at (a) $t = 2$, (b) 4, and (c) 6 for four different resolutions: $n_g = 32$ (black), 64 (blue), 128 (red) and 256 (magenta)
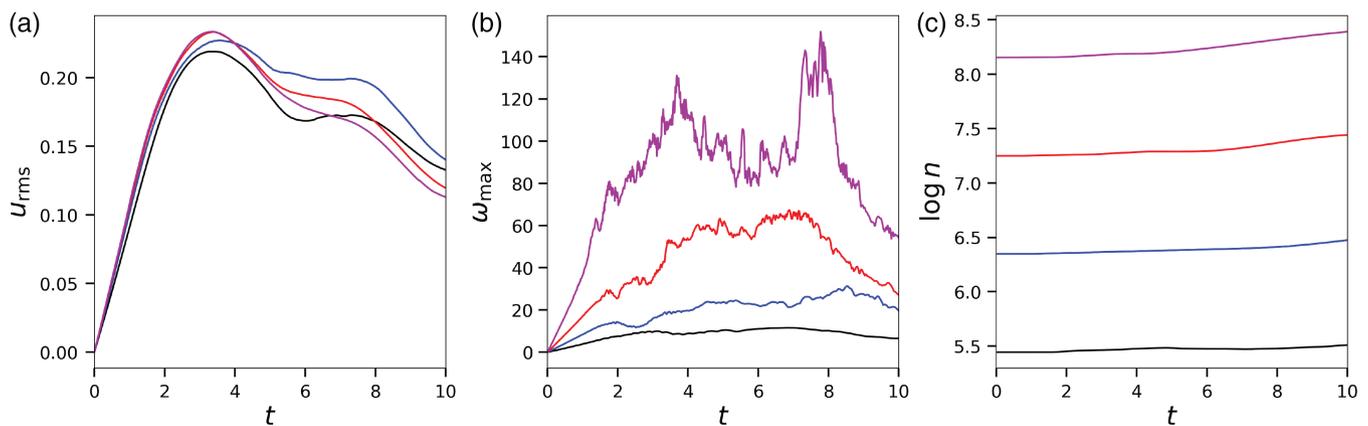
FIGURE 13   Time evolution of (a) the r.m.s. velocity, (b) the maximum vorticity magnitude and (c) the number of parcels, for four different resolutions: $n_g = 32$ (black), 64 (blue), 128 (red) and 256 (magenta)

MPIC model may facilitate the study and understanding of these processes in real clouds.

To understand what MPIC may offer for resolving clouds in global models, Figure 16 shows the cloud amount captured at low resolutions, specifically $n_g = 8$, 16 and 32. All resolutions exhibit cloud formation, albeit without any of the fine detail seen at higher resolutions in Figure 15. Nevertheless, the ability of MPIC to capture cloud formation at such coarse resolutions is promising.

4.10 | Comparison with MONC

In this paper, we have tested only the internal consistency of the MPIC model. A detailed comparison with an entirely different numerical model, the Met Office/NERC cloud model (MONC), is the focus of Böing *et al.* (forthcoming). Here we simply illustrate how well MPIC compares with MONC. Not one aspect of the methods used in the two models is similar, except that both models attempt to solve the same equations and start with the same initial condition. MONC employs either a TVD (total variation diminishing) advection scheme or a Smagorinsky subgrid model

to control small-scale motions (full details are available in Böing *et al.*, forthcoming). MONC uses finite differences on a staggered grid, and takes velocity, buoyancy and specific humidity to be the prognostic variables, and is entirely Eulerian.

Given the substantial differences in model formulations, the results shown in Figure 17 display surprisingly close correspondence. This figure zooms in on part of the domain at $t = 6$, with results for two MONC simulations at 1024^3 resolution using different subgid models, and for an MPIC simulation at 384^3 resolution showing both reconstructed and gridded fields. (Note that the vertical} velocity w is available only on the grid.) Overall, the comparison is excellent, though details differ as expected in a highly turbulent flow such as this. The vorticity amplitudes in MPIC are substantially higher than in MONC, due to MPIC's explicit subgrid representation. In other words, MPIC can carry substantially more information at small scales despite using a coarser grid resolution (this is examined further in Böing *et al.*, forthcoming). Notably, the differences in the two MONC simulations are comparable to the differences between the MONC and the MPIC simulation.
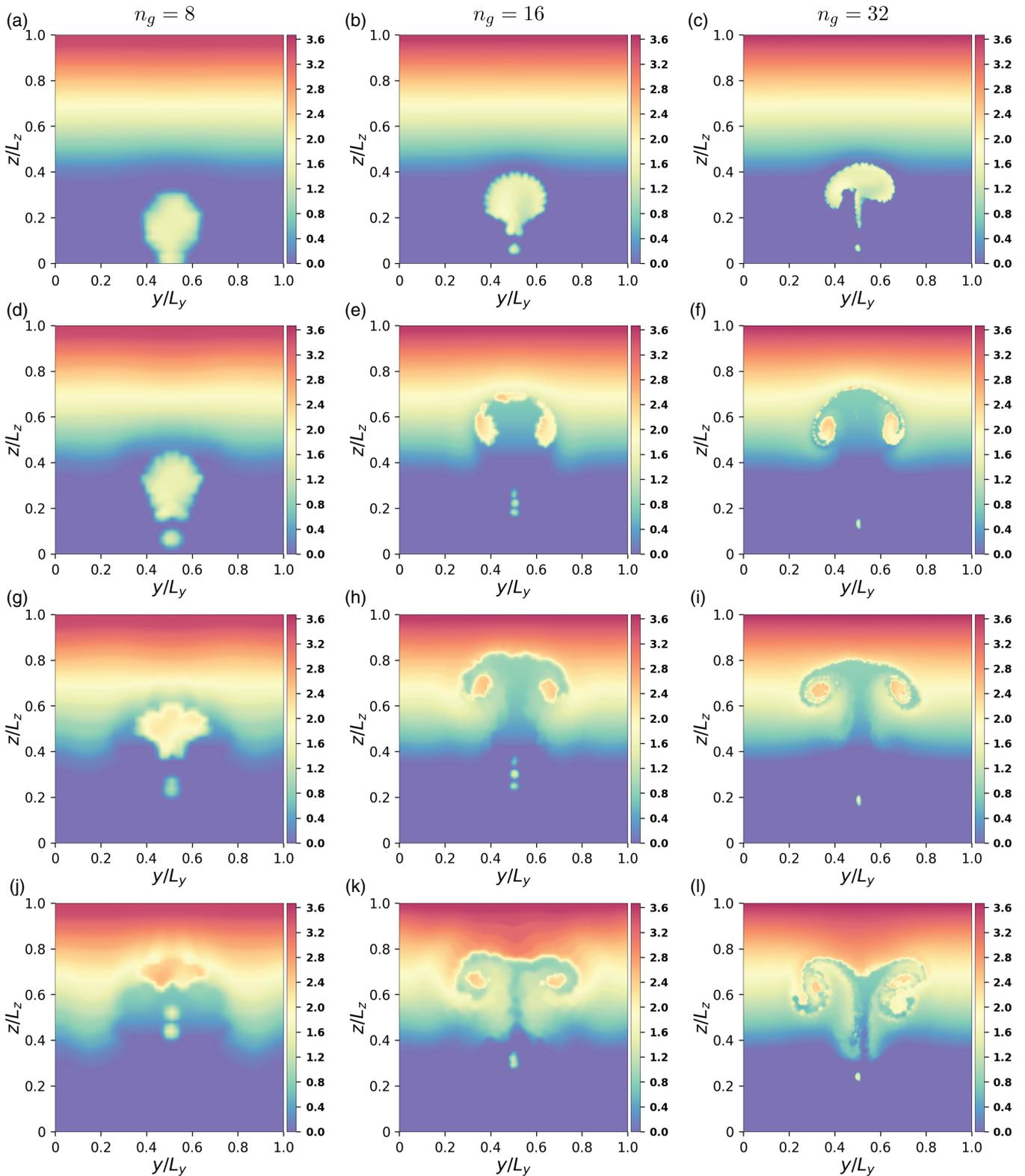
FIGURE 14 Comparison of the total buoyancy b at t = (a–c) 2, (d–f) 4, (g–i) 6 and (j–l) 8, for resolutions n_g = (a, d, g, j) 8, (b, e, h, k) 16 and (c, f, l) 32

5 | CONCLUSIONS

In this paper, we have outlined and tested a noncon-ventional, alternative numerical method for modelling moist atmospheric convection. The proposed "Moist Parcel-In-Cell" (MPIC) model is currently only a prototype for modelling real convection, and has been developed in an

idealized manner simply to demonstrate its potential in this context. In a forthcoming paper (Böing *et al.*, forthcoming), we carry out a detailed comparison of the MPIC model with a conventional convection-permitting model, the Met Office/NERC cloud model (MONC). There, we show that MPIC offers distinct advantages primarily due to its
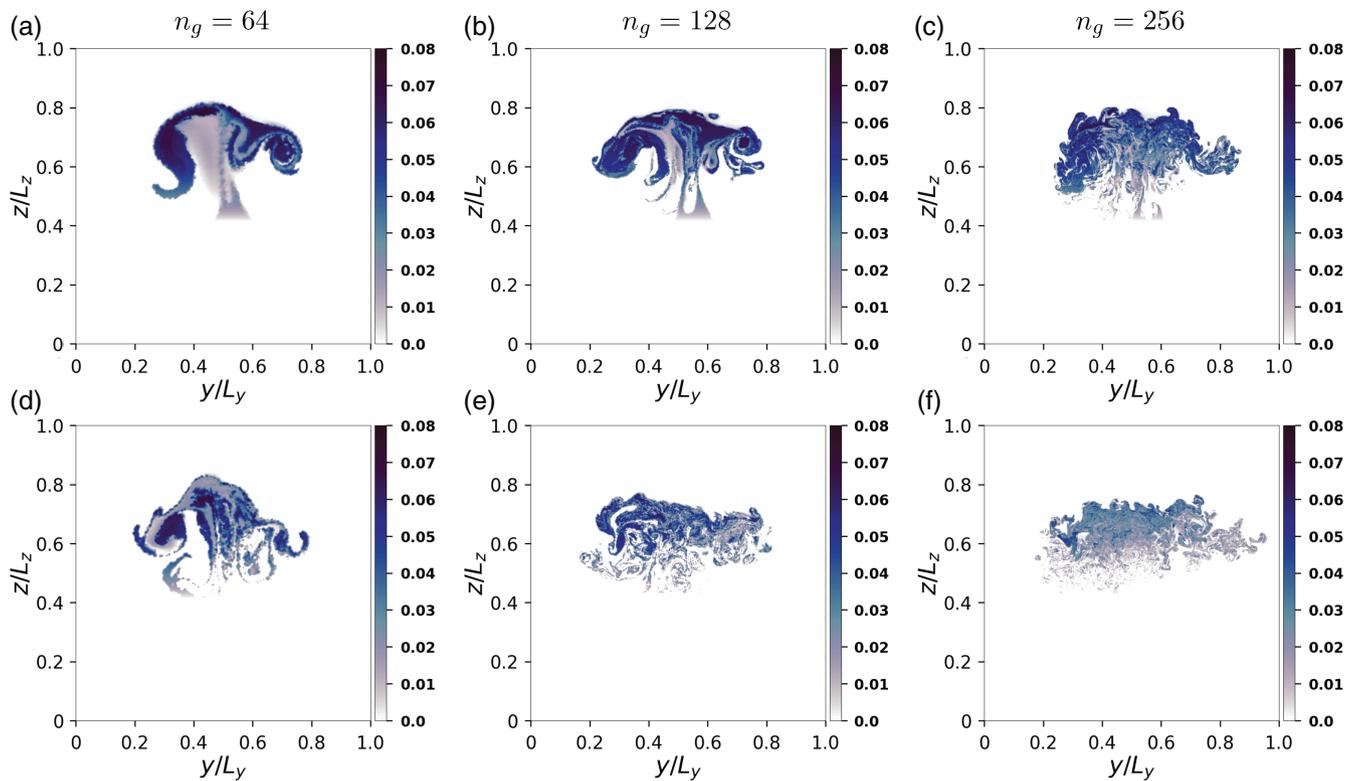
FIGURE 15 Comparison of the condensed portion $\widetilde{q}_c$ of the specific humidity (nominal cloud amount) at $t =$ (a–c) 6 and (d–f) 8, for resolutions $n_g =$ (a, d) 64, (b, e) 128 and (c, f) 256
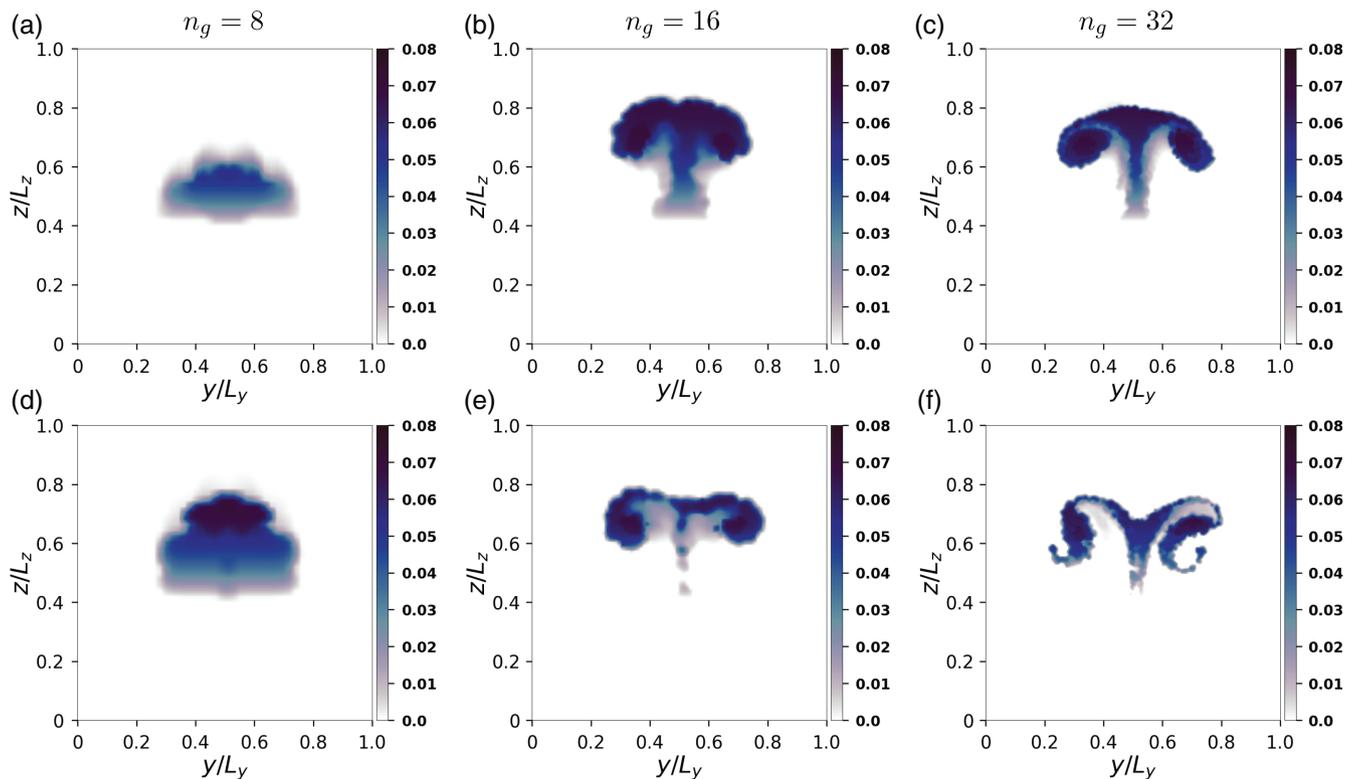
FIGURE 16 As Figure 15, but for resolutions $n_g =$ (a, d) 8, (b, e) 16, and (c, f) 32

explicit subgrid model of convection and its exceptionally weak numerical diffusion.

To facilitate further realistic developments of the model, the next step is to incorporate MPIC into MONC as both an alternative advection scheme and an alternative dynamical core. This will enable full parallelization of the model, permit studies at higher resolution, and allow access to a number of useful design features in MONC.
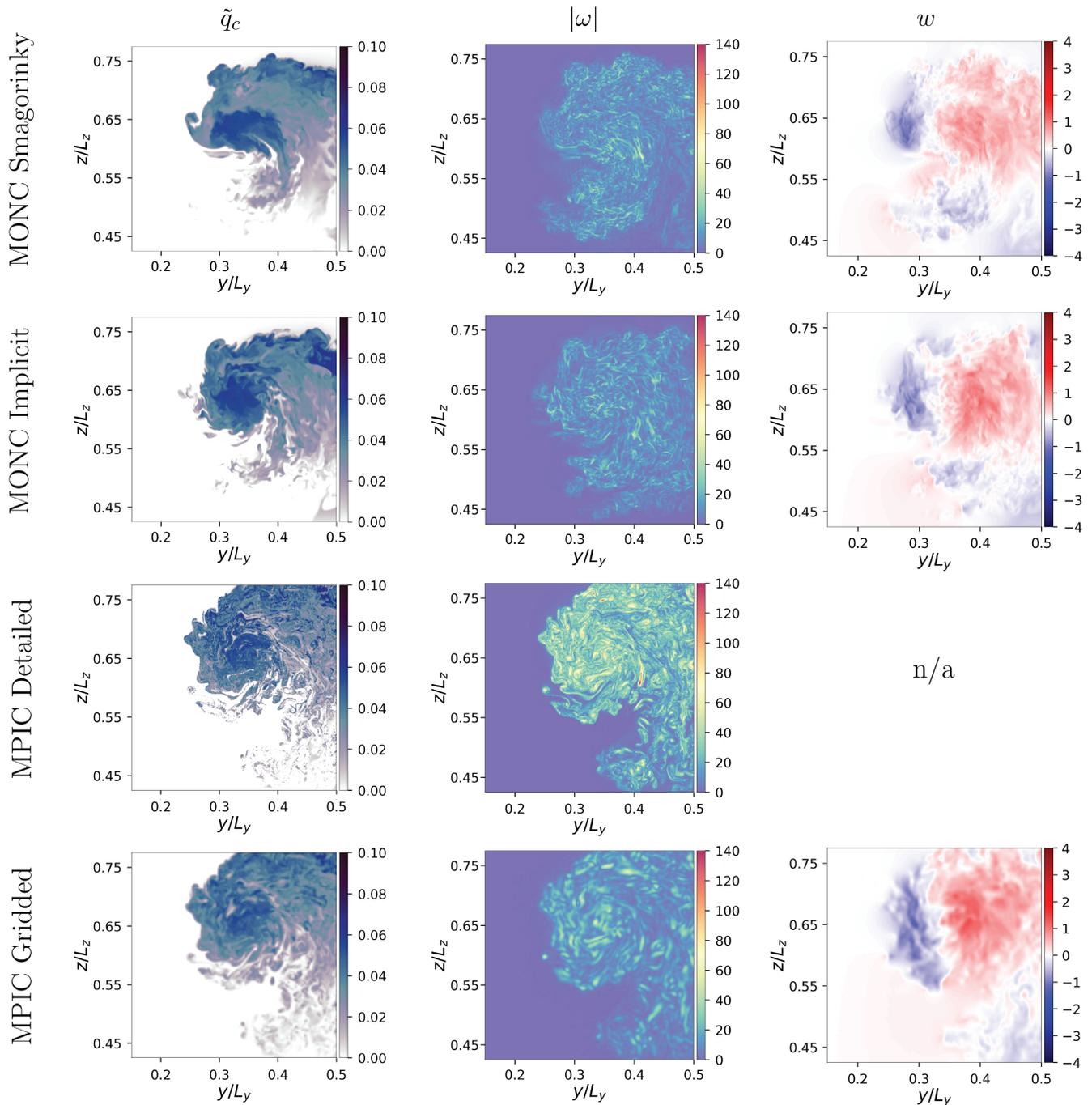
FIGURE 17 (a, d, g, j) Liquid water cloud amount $\tilde{q_c}$, (b, e, h, k) magnitude of the vorticity $\|\boldsymbol{\omega}\|$ and (c, f, i, l) vertical velocity w in MONC and MPIC at $t = 6$. Only part of the domain is shown. For MPIC, both (j, k, l) grid scale fields and (g, h, i) fields reconstructed using a detailed interpolation algorithm are shown

There are a number of extensions under consideration. A priority is to replace the present idealized formulation of saturation specific humidity with a more accurate pressure/temperature-dependent formulation. Another priority| is to allow for surface heating and moisture fluxes, to enable studies of sustained or cyclic convection. We also plan to relax the incompressible Boussinesq approximation to permit a more accurate treatment of deep convection, either by an anelastic formulation or a fully compressible one. Finally, we are currently attempting to include cloud microphysical processes by evolving a droplet size distribution and including a description of precipitation.

ACKNOWLEDGEMENTS

ORCID

David G. Dritschel ⬤ orcid.org/0000-0001-6489-3395

REFERENCES

Aksman, M., Novikov, E. and Orszag, S. (1985) Vorton method in three-dimensional hydrodynamics. *Physical Review Letters*, 54(22), 2410–2413.

Alkemade, A., Nieuwstadt, F. and van Groesen, E. (1993) The vorton method. *Applied Scientific Research*, 51(1), 3–7.

Anderson, C. and Greengard, C. (1985) On vortex methods. *SIAM Journal of Numerical Analysis*, 22, 413–440.

Andrejczuk, M., Reisner, J.M., Henson, B., Dubey, M.K. and Jeffery, C.A. (2008) The potential impacts of pollution on a nondrizzling stratus deck: does aerosol number matter more than type? *Journal of Geophysical Research: Atmospheres*, 113(D19204). https://doi.org/10.1029/2007JD009445.

Austin, P., Baker, M., Blyth, A.M. and Jensen, J. (1985) Small-scale variability in warm continental cumulus clouds. *Journal of the Atmospheric Sciences*, 42(11), 1123–1138.

Blyth, A.M., Bennett, L. and Collier, C.G. (2015) High-resolution observations of precipitation from cumulonimbus clouds. *Meteorological Applications*, 22(1), 75–89.

Blyth, A.M., Lasher-Trapp, S. and Cooper, W. (2005) A study of thermals in cumulus clouds. *Quarterly Journal of the Royal Meteorological Society*, 131, 1171–1190.

Blyth, A.M., Lowenstein, J., Huang, Y., Cui, Z., Davies, S. and Carslaw, K. (2013) The production of warm rain in shallow maritime cumulus clouds. *Quarterly Journal of the Royal Meteorological Society*, 139, 20–31.

Böing, S.J., Dritschel, D.G., Parker, D.J. and Blyth, AM. (forthcoming) Comparison of the Moist Parcel-In-Cell (MPIC) method with a large-eddy simulation of a cloud. *Quarterly Journal of the Royal Meteorological Society*.

Bony, S., Stevens, B., Frierson, D., Jakob, C., Kageyama, M., Pincus, R., Shepherd, T., Sherwood, S., Siebesma, AP., Sobel, A., Watanabe, M. and Webb, M. (2015) Clouds, circulation and climate sensitivity. *Nature Geosciences*, 8, 261–268.

Brackbill, J. and Ruppel, H. (1986) FLIP: a method for adaptively zoned, particle in cell calculations of fluid flows in two dimensions. *Journal of Computational Physics*, 65, 314–343.

Bretherton, C. and Smolarkiewicz, P. (1989) Gravity waves, compensating subsidence and detrainment around cumulus clouds. *Journal of the Atmospheric Sciences*, 46(6), 740–759.

Brown, A.R., Cederwall, R.T., Chlond, A., Duynkerke, P.G., Golaz, J.-C., Khairoutdinov, M., Lewellen, D.C., Lock, A.P., MacVean, M.K., Moeng, C.-H., Neggers, R.A.J., Siebesma, A.P. and Stevens, B. (2002) Large-eddy simulation of the diurnal cycle of shallow cumulus convection over land. *Quarterly Journal of the Royal Meteorological Society*, 128(582), 1075–1093.

Canuto, C., Hussaini, M., Quarteroni, A. and Zang, T. (2007) *Spectral Methods*. Berlin: Springer.

Christiansen, J. and Zabusky, N. (1973) Instability, coalescence and fission of finite-area vortex structures. *Journal of Fluid Mechanics*, 61, 219–243.

Cooper, W., Lasher-Trapp, S. and Blyth, AM. (2013) The influence of entrainment and mixing on the initial formation of rain in a warm cumulus cloud. *Journal of the Atmospheric Sciences*, 70(6), 1727–1743.

Cottet, G.H. and Koumoutsakos, P. (2000) *Vortex Methods: Theory and Practice*. Cambridge: Cambridge University Press.

Davidson, P. (2015) *Turbulence: An Introduction for Scientists and Engineers*. Oxford: Oxford University Press.

Deardorff, J. (1980) Stratocumulus-capped mixed layers derived from a three-dimensional model. *Boundary-Layer Meteorology*, 18(4), 495–527.

Dritschel, D.G. and Ambaum, M. (1997) A contour-advective semi-Lagrangian numerical algorithm for simulating fine-scale conservative dynamical fields. *Quarterly Journal of the Royal Meteorological Society*, 123, 1097–1130.

Dritschel, D.G. and Fontane, J. (2010) The combined Lagrangian advection method. *Journal of Computational Physics*, 229, 5408–5417.

Dritschel, D.G. and Scott, R. (2009) On the simulation of nearly inviscid two-dimensional turbulence. *Journal of Computational Physics*, 228, 2707–2711.

Dritschel, D.G. and Tobias, S. (2012) Two-dimensional magnetohydrodynamic turbulence in the small Prandtl number limit. *Journal of Fluid Mechanics*, 703, 85–98.

Durran, D. and Arakawa, A. (2007) Generalizing the Boussinesq approximation to stratified compressible flow. *Comptes Rendus Mécanique*, 335, 655–664.

Fontane, J. and Dritschel, D.G. (2009) The HyperCASL algorithm: a new approach to the numerical simulation of geophysical flows. *Journal of Computational Physics*, 228, 6411–6425.

Frank, J., Gottwald, G. and Reich, S. (2002) A Hamiltonian particle-mesh method for the rotating shallow-water equations. In: Griebel M. and Schweitzer M.A. (Eds.) *Meshfree Methods for Partial Differential Equations*, Lecture Notes in Computational Science and Engineering Vol. 26. Berlin: Springer, pp. 131–142.

Gadian, A.M. (1991) Lagrangian modelling of an atmospheric plume and an analysis of the comparative advantages of Lagrangian and Eulerian methods. In: Farmer D.G. and Rycroft M.J. (Eds.) *Computer Modelling in Environmental Sciences*. Oxford: Oxford University Press, pp. 255–273.

Grabowski, W.W. and Clark, T. (1993) Cloud-environment interface instability. Part II: extension to three spatial dimensions. *Journal of the Atmospheric Sciences*, 50(4), 555–573.

Grabowski, W.W., Dziekan, P. and Pawlowska, H. (2018) Lagrangian condensation microphysics with Twomey CCN activation. *Geoscientific Model Development*, 11, 103–120.

Grabowski, W.W. and Smolarkiewicz, P. (1999) CRCP: a cloud resolving convection parameterization for modeling the tropical convecting atmosphere. *Physica D: Nonlinear Phenomena*, 133(1), 171–178.

Grabowski, W.W. and Smolarkiewicz, P. (2002) A multiscale anelastic model for meteorological research. *Monthly Weather Review*, 130(4), 939–956.

Grewe, V., Brinkop, S., Jöckel, P., Shin, S., Reich, S. and Yserentant, H. (2014) On the theory of mass conserving transformations for Lagrangian methods in 3D atmospheric-chemistry models. *Meteorologische Zeitschrift*, 23(4), 441–447.

Heinze, R., Mironov, D. and Raasch, S. (2015) Second-moment budgets in cloud topped boundary layers: a large-eddy simulation study. *Journal of Advances in Modeling Earth Systems*, 7(2), 510–536.

Heymsfield, A., Johnson, P. and Dye, J. (1978) Observations of moist adiabatic ascent in Northeast Colorado cumulus congestus clouds. *Journal of the Atmospheric Sciences*, 35(9), 1689–1703.

Holloway, C., Petch, J., Beare, R., Bechtold, P., Craig, G., Derbyshire, S., Donner, L., Field, P., Gray, S., Marsham, J., Parker, D.J., Plant, R., Roberts, N., Schultz, D., Stirling, A. and Woolnough, S. (2014) Understanding and representing atmospheric convection across scales: recommendations from the meeting held at Dartington hall, Devon, UK, 28–30 January 2013. *Atmospheric Science Letters*, 15(4), 348–353.

Khairoutdinov, M.F., Krueger, S.K., Moeng, C.-H., Bogenschutz, P.A. and Randall, D.A. (2009) Large-eddy simulation of maritime deep tropical convection. *Journal of Advances in Modeling Earth Systems*, 1(4). https://doi.org/10.3894/JAMES.2009.1.15.

Klinger, M., Leinen, P. and Yserentant, H. (2005) The finite mass method on domains with boundary. *SIAM Journal on Scientific Computing*, 26, 1744–1759.

Matheou, G. (2011) On the fidelity of large-eddy simulation of shallow precipitating cumulus convection. *Monthly Weather Review*, 139(9), 2918–2939.

McKiver, W. and Dritschel, DG. (2003) The motion of a fluid ellipsoid in a general uniform background flow. *Journal of Fluid Mechanics*, 474, 147–173.

Meneveau, C. and Katz, J. (2000) Scale-invariance and turbulence models for large-eddy simulation. *Annual Review of Fluid Mechanics*, 32(1), 1–32.

Monaghan, J. (1992) Smoothed particle hydrodynamics. *Annual Review of Astronomy and Astrophysics*, 30(1), 543–574.

Moser, D. and Lasher-Trapp, S. (2017) The influence of successive thermals on entrainment and dilution in a simulated cumulus congestus. *Journal of the Atmospheric Sciences*, 74(2), 375–392.

Novikov, E. (1983) Generalized dynamics of three-dimensional vortical singularities (vortons). *Soviet Physics JETP*, 57(3), 566–569.

Pauluis, O. (2008) Thermodynamic consistency of the anelastic approximation for a moist atmosphere. *Journal of the Atmospheric Sciences*, 65(8), 2719–2729.

Pauluis, O. and Schumacher, J. (2010) Idealized moist Rayleigh–Bénard convection with piecewise linear equation of state. *Communications in Mathematical Sciences*, 8(1), 295–319.

Petch, J., Blossey, P. and Bretherton, C. (2008) Differences in the lower troposphere in two- and three-dimensional cloud-resolving model simulations of deep convection. *Quarterly Journal of the Royal Meteorological Society*, 134, 1941–1946.

Pierrehumbert, R.T., Brogniez, H. and Roca, R. (2007) On the relative humidity of the Earth's atmosphere. In: Schneider T. and Sobel A.H. (Eds.) *The Global*

Circulation of the Atmosphere. Princeton, NJ: Princeton University Press, pp. 143–185.

Pope, S.B. (2004) Ten questions concerning the large-eddy simulation of turbulent flows. *New Journal of Physics*, 6. https://doi.org/10.1088/1367-2630/6/1/035.

Pressel, K., Kaul, C., Schneider, T., Tan, Z. and Mishra, S. (2015) Large-eddy simulation in an anelastic framework with closed water and entropy balances. *Journal of Advances in Modeling Earth Systems*, 7(3), 1425–1456.

Redelsperger, J.-L., Brown, PRA., Guichard, F., How, C., Kawasima, M., Lang, S., Montmerle, T., Nakamura, K., Saito, K., Seman, C., Tao, W.K. and Donner, L.J. (2000) A GCSS model intercomparison for a tropical squall line observed during TOGA-COARE. I: cloud-resolving models. *Quarterly Journal of the Royal Meteorological Society*, 126, 823–863.

Riechelmann, T., Noh, Y. and Raasch, S. (2012) A new method for large-eddy simulations of clouds with Lagrangian droplets including the effects of turbulent collision. *New Journal of Physics*, 14. https://doi.org/10.1088/1367-2630/14/6/065008.

Schalkwijk, J., Jonker, H., Siebesma, A. and Van Meijgaard, E. (2015) Weather forecasting using GPU-based large-eddy simulations. *Bulletin of the American Meteorological Society*, 96(5), 715–723.

Seifert, A., Heus, T., Pincus, R. and Stevens, B. (2015) Large-eddy simulation of the transient and near-equilibrium behavior of precipitating shallow convection. *Journal of Advances in Modeling Earth Systems*, 7(4), 1918–1937.

Shima, S., Kusano, K., Kawano, A., Sugiyama, T. and Kawahara, S. (2009) The super-droplet method for the numerical simulation of clouds and precipitation: a particle-based and probabilistic microphysics model coupled with a non-hydrostatic model. *Quarterly Journal of the Royal Meteorological Society*, 135, 1307–1320.

Shipton, J. (2008) *Balance, gravity waves and jets in turbulent shallow water flows*. PhD thesis, University of St Andrews, School of Mathematics and Statistics. St Andrews Research Repository at http://hdl.handle.net/10023/708; accessed 1 September 2018

Shutts, G.J. and Allen, T. (2007) Sub-gridscale parametrization from the perspective of a computer games animator. *Atmospheric Science Letters*, 8(4), 85–92.

Siebesma, AP., Bretherton, C., Brown, A., Chlond, A., Cuxart, J., Duynkerke, P., Jiang, H., Khairoutdinov, M., Lewellen, D., Moeng, C.H., Sanchez, E., Stevens, B. and Stevens, D. (2003) A large-eddy simulation intercomparison study of shallow cumulus convection. *Journal of the Atmospheric Sciences*, 60(10), 1201–1219.

Siebesma, A.P. and Cuijpers, J. (1995) Evaluation of parametric assumptions for shallow cumulus convection. *Journal of the Atmospheric Sciences*, 52(6), 650–666.

Smilgys, R. and Bonnell, I. (2017) Formation of stellar clusters. *Monthly Notices of the Royal Astronomical Society*, 472(4), 4982–4991.

Sommeria, G. (1976) Three-dimensional simulation of turbulent processes in an undisturbed trade wind boundary layer. *Journal of the Atmospheric Sciences*, 33(2), 216–241.

Tsang, Y.K. and Vanneste, J. (2017) The effect of coherent stirring on the advection–condensation of water vapour. *Proceedings of the Royal Society A*, 473(20170), 196.

Twomey, S. (1966) Computations of rain formation by coalescence. *Journal of the Atmospheric Sciences*, 23(4), 405–411.

Wyszogrodzki, A., Grabowski, W.W., Wang, L.P. and Ayala, O. (2013) Turbulent collision–coalescence in maritime shallow convection. *Atmospheric Chemistry and Physics*, 13, 8471–8487.